Reactive absorption of CO2 in NaOH: An Euler-Euler simulation study

Krauß, M.; Rzehak, R.;

Originally published:

January 2018

Chemical Engineering Science 181(2018), 199-214

DOI: https://doi.org/10.1016/j.ces.2018.01.009

Perma-Link to Publication Repository of HZDR:

https://www.hzdr.de/publications/Publ-25445

Reactive absorption of CO_2 in NaOH: An Euler-Euler simulation study

Manuel Krauß[1,2], Roland Rzehak[1*]
[1] Helmholtz-Zentrum Dresden – Rossendorf, Institute of Fluid Dynamics, Bautzner Landstrasse 400, D-01328 Dresden, Germany
[2] Technische Universität Dresden, Chair of Chemical Reaction Engineering and Process Plant, Münchnerplatz 3, D-01062 Dresden, Germany

Abstract

In a pioneering study, Darmana et al. [Chemical Engineering Science 62 (2007), 2556 - 2575], considered a simulation model for the reactive absorption of CO_2 in aqueous NaOH in a bubble column. Although quite good agreement with measured data was obtained, two shortcomings of the model can be identified: (i) use of an approximate expression for the enhancement factor outside its range of validity and (ii) neglect of the reaction of CO_2 with water. Herein, Euler-Euler / RANS simulations are presented that improve on these aspects. Comparison with both the experiment and the Euler-Lagrange / LES simulations of Darmana et al. (2007) shows the need to further increase the accuracy of the fluid dynamic part of the present model.

Keywords: mass transfer, chemical reaction, chemisorption, enhancement factor, dispersed gas-liquid multiphase flow, Euler-Euler two-fluid model, CFD simulation

[*] Corresponding author email: r.rzehak@hzdr.de

1 INTRODUCTION

Mass transfer from gas bubbles to the surrounding liquid or vice versa is an important consideration in chemical engineering. Such absorption or desorption processes frequently occur in the presence of a chemical reaction in the liquid phase. To distinguish non-reactive and reactive processes, one refers to physisorption and chemisorption, respectively. Physisorption is commonly described by a mass transfer coefficient which relates the mass flux to a concentration difference and is a function of material properties and flow conditions. The effect of a chemical reaction is usually taken into account by an enhancement factor, which depends on type, order, and rates of the reaction.

Compared with fluid dynamics of bubbly flows, the modeling of mass transfer is much less developed, in particular for the reactive case. For simulations on the scale of technical equipment the Eulerian framework of multiphase flow has to be used. This requires closure relations for the mass transfer coefficient and in the reactive case also for the enhancement factor. The number of studies proposing such models and assessing their performance is quite limited.

Simulation studies of chemisorption in bubbly flows have been carried out mostly for absorption of CO_2 in aqueous NaOH or KOH (Jain et al., 2015; Gruber et al., 2015; Zhang et al., 2009; Darmana et al., 2007; Bauer and Eigenberger, 2000, 1999; Marquez et al., 1999; Fleischer et al., 1996) and ozonation of water (Gong et al., 2007; Cockx et al., 1999). Lab scale bubble columns were considered in Jain et al. (2015), Gruber et al. (2015), Zhang et al. (2009), Darmana et al. (2007), Bauer and Eigenberger (2000, 1999), Fleischer et al. (1996), a lab-scale airlift-column with external loop in Marquez et al. (1999), and a baffled ozonation tower of industrial size in Cockx et al. (1999). Gong et al. (2007) investigated a single bubble plume. A fully 3D treatment by the Euler-Euler approach has been applied in Zhang et al. (2009) and Cockx et al. (1999). Bauer and Eigenberger (2000, 1999) have used a multiscale approach where a detailed simulation of the fluid-dynamics was coupled with a coarse model for the reactive mass transfer. 1D Euler-Euler simulations have been performed in Marquez et al. (1999) and Fleischer et al. (1996). The Euler-Lagrange approach, again in three dimensions, was employed in Jain et al. (2015), Gruber et al. (2015), Darmana et al. (2007) and Gong et al. (2007). Turbulence was included by means of a RANS model in Cockx et al. (1999). Jain et al. (2015), Gruber et al. (2015), Zhang et al. (2009), and Darmana et al. (2007) used an LES treatment. In the simplified approaches of Bauer and Eigenberger (2000, 1999), Marquez et al. (1999), Fleischer et al. (1996) and the Euler-Lagrange simulation of Gong et al. (2007) turbulence was not considered explicitly.

Progress in simulation studies is hampered by a shortage of validation data. This in turn is related to the difficulty of concentration measurements. Sum-parameters like pH, conductivity, or in the presence of significant reaction heat also temperature are broadly applicable, but track only the overall progress of the reaction. If the transfer rate is high enough, the axial development of bubble size or gas fraction provides indirect information of this kind. Optical techniques such as Raman, Infrared, or UV-VIS spectroscopy in principle allow to follow individual species concentrations, but specific recipes have to be worked out for each application.

Darmana et al. (2007) compared their simulations with own measurements of time-dependent pH-value at a single location in the column and an axial profile of mean bubble size. Bauer and Eigenberger (2000) and Fleischer et al. (1996) used data from Becker (1996), who provided time-dependent pH-value and temperature at four different heights in a bubble column for the reactive absorption of CO_2 in NaOH. A comparison of the simulations with own measurements of average dissolved ozone at five different locations in the ozonation tower was given by Cockx et al. (1999). Validation by own measurements of average gas

fraction profiles was provided by Marquez et al. (1999). No validation for the mass transfer part was shown in the simulation studies of Jain et al. (2015), Gruber et al. (2015), Zhang et al. (2009) and Gong et al. (2007).

A rather detailed model for the reaction kinetics and physico-chemical properties of the solution was presented by Darmana et al. (2007) together with expressions for the enhancement factor, mass transfer coefficient and effective diffusivity. Mostly the same models were used in the later works of Jain et al. (2015), Gruber et al. (2015) and Zhang et al. (2009). While the achieved level of agreement with the data was quite encouraging, the modeling implied some approximations which are not suited for the problem at hand as has been investigated in detail in a previous study (Krauß and Rzehak, 2016).

The results of Krauß and Rzehak (2016) were obtained by means of a simplified description of the hydrodynamic phenomena in the bubble column, which applies locally at the point of measurement. In this way, possible errors of the present hydrodynamic modeling were excluded so that the description of the chemistry could be assessed in isolation. It was shown that an approximation for the asymptotic limit of the enhancement factor in case of an instantaneous irreversible second order reaction, which appears frequently in chemical engineering textbooks (e.g. Westerterp et al., 1987), and was used throughout the works quoted above, is restricted to situations with a larger enhancement effect than that occurring under the conditions of the experiment of Darmana et al. (2007). An improved fit formula with a rather wide range of application was presented. In addition, it was shown that the later stage of the neutralization process cannot be described correctly only by the reaction between CO_2 and hydroxide ions, but the reaction of CO_2 with water needs to be taken into account as well. This second reaction pathway was neglected in the above works.

For the present contribution, full Euler-Euler / RANS simulations have been conducted making use of the improved expression for the enhancement factor and the full reaction model including both the hydroxide and the water pathways. The results are compared with both the measurements and Euler-Lagrange / LES simulations of Darmana et al. (2007) and also the simplified pointwise model of Krauß and Rzehak (2016).

A summary of the experimental and simulation results of Darmana et al. (2007) is given in section 2. The Euler-Euler / RANS modeling of reactive mass transfer used in the present work is described in section 3. Results of the calculations are presented in section 4 and compared to the aforementioned works. Conclusions and an outlook are given in section 5. Two appendices contain the correlations for reaction kinetics and physico-chemical properties that were used and a fit formula for the enhancement factor of an instantaneous irreversible second order reaction developed in our previous work (Krauß and Rzehak 2016).

2 SUMMARY OF RESULTS FROM DARMANA ET AL. (2007)

Darmana et al. (2007) investigated a lab scale bubble column of 200 mm width and 30 mm depth as sketched in Figure 1. Initially the column was filled with liquid up to a level of 1000 mm. Gas was supplied through 21 needles arranged with a square pitch of 5 mm in the center of the column bottom. A first experiment was performed to study the hydrodynamic behavior without any reaction by using N_2 as the gas. A second experiment then focussed on the reactive mass transfer during chemisorption of CO_2. As the liquid an aqueous NaOH solution at an initial pH of 12.5 was used for both cases. To clearly show the effects of the reactive absorption on the hydrodynamics, N_2 gas was supplied in the second experiment until a statistically steady state had developed and then the gas supply was switched to CO_2. In both cases the gas superficial velocity was 0.007 m/s. The size of the generated bubbles right at the needles was d_B = 5.5 mm. The resulting integral gas fractions (see
Table **1**) are small enough so the rise in liquid level can be neglected. The precise value of the temperature in the experiments was not reported.
In both experiments bubble velocity was measured by PIV. Profiles of average axial bubble velocity over the entire width of the column at a height of y = 750 mm are reported as well as time-dependent values at a single point x = -50 mm, y = 500 mm, z = 0 mm. By means of a Fourier transform the frequency of bubble plume oscillations was determined. The integral gas holdup was simply obtained from the difference of the liquid heights with and without aeration.
For the reactive case additional measurements of bubble size and pH-value were taken. Bubble size was measured by videometry. An axial profile of the average bubble size in the center of the column is reported. Values up to a height of approximately 400 mm were judged as unreliable. In this region most bubbles appeared as clusters which could not be handled by the sizing algorithm, resulting in underestimated sizes. The pH-value was measured by a glass electrode at a single point located 2 cm below the liquid surface in the center of the column, i.e. at the point x = 0 mm, y = 980 mm, z = 0 mm. Time-dependent values at this point are provided.
In addition to the experiment, Darmana et al. (2007) also presented simulation results for both the non-reactive and reactive case using an Euler-Lagrange / LES method. A comparison of results for some integral properties of the flow is shown in
Table **1**. Local values will be considered in section 4 together with results from the present Euler-Euler / RANS simulations.

	non-reactive case		reactive case	
	α_G	f_{plume}	α_G	f_{plume}
experiment	2.3 %	0.17 Hz	1.2 %	0.10 Hz
simulation	2.2 %	0.17 Hz	1.6 %	0.15 Hz

Table 1: Integral gas holdup and bubble plume oscillation frequency of the experiment and the simulation of Darmana et al. (2007).

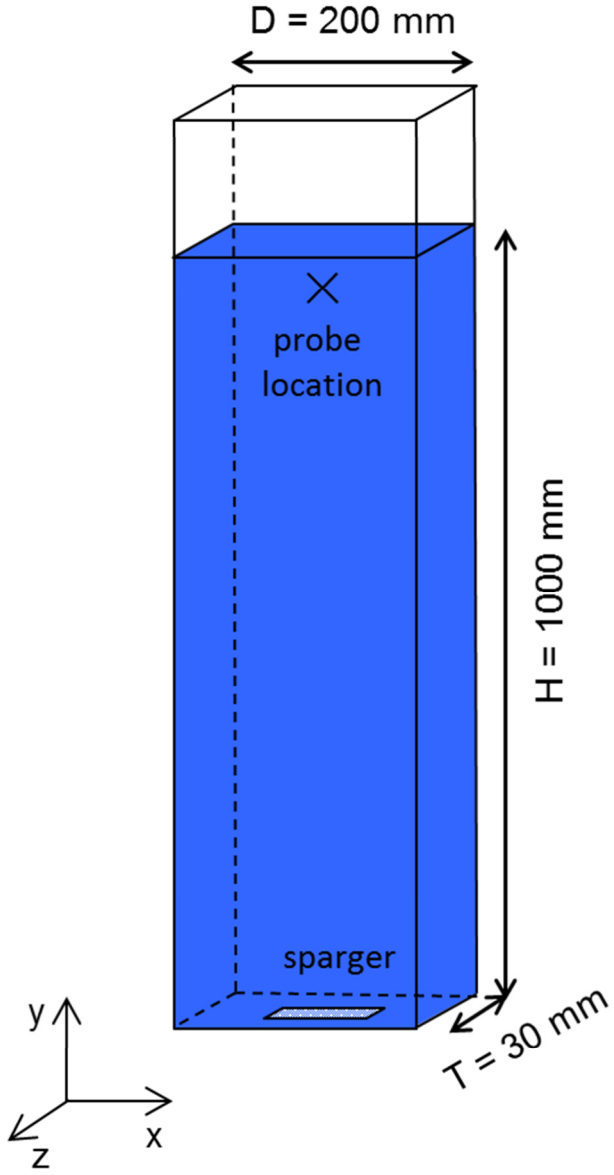

Figure 1: Sketch of geometry for the test from Darmana et al. (2007). The origin of coordinates is taken in the center of the column bottom.

3 EULER-EULER MODELING OF REACTIVE MASS TRANSFER

An Euler-Euler model for the fluid dynamical part of the problem has been developed and validated in a number of previous studies (Rzehak and Krepper, 2013; Rzehak et al., 2014; Ziegenhein et al., 2015; Rzehak and Kriebitzsch, 2015; Rzehak and Krepper, 2015; Rzehak et al., 2015; Liao et al., 2016; Rzehak et al., 2016, 2017; Ziegenhein et al, 2017). In this model, momentum exchange between the phases is governed by drag, lift, wall, turbulent dispersion and virtual mass forces. Turbulence is described by a two-equation RANS model augmented by source terms describing the bubble-induced contribution to the liquid turbulence. Since the complete fluid dynamical model has been amply described before, we here focus on the extensions necessary to include mass transfer and chemical reaction. The description is kept rather general at first, some simplifications are introduced later on. Specifications for the reactive absorption of CO_2 in aqueous NaOH are given in Table 2 below.

3.1 Balance equations for species transport and fluid dynamics

Since the use of different units for the concentration of a species *X* is customary in fluid dynamics and chemical engineering, namely mass concentration ρ^X and molar concentration C^X as well as corresponding mass fractions Y^X and mole fractions X^X, their relations are presented in detail first. With the molar mass M^X of species *X*, we have

$$\rho^X = M^X C^X . \tag{1}$$

Introducing the mass concentration $\rho = \sum_X \rho^X$ of the multi-component mixture and its molar counterpart $C = \sum_X C^X$, furthermore

$$Y^X = \rho^X / \rho , \tag{2}$$

$$X^X = C^X / C . \tag{3}$$

Interconversion between mass and mole fractions is facilitated by the relation

$$Y^X = \frac{M^X}{M} X^X , \tag{4}$$

where *M* is the mixture molar mass given by the equivalent relations

$$M = \sum_X X^X M^X \qquad ; \qquad \frac{1}{M} = \sum_X \frac{Y^X}{M^X} . \tag{5}$$

Finally note that the mass concentration of each species in the mixture has to be distinguished from its thermodynamic density as a pure substance, which will be denoted as $\tilde{\rho}^X$.

To capture the shrinkage of the gas bubbles the homogeneous multiple size group (MUSIG) model (Lo, 2000) is applied, which is sometimes also called the class method or sectional method (Ramkrishna, 2000). In this approach the dispersed phase is divided into several size groups. Frequently the group definitions are based on bubble mass rather than size to ensure mass conservation. The relation between both is given by

$$d_i = \left(\frac{6}{\pi} \frac{m_i}{\rho_G} \right)^{1/3} . \tag{6}$$

In accordance with common denominations we use the term size group in either case.

In a multi-component system, transport equations are needed for the concentration of each chemical species *X*, which may be present in both the liquid and gas phase. For each size group *i = 1 ... M* of the gas phase and for the liquid phase these transport equations are

$$\frac{\partial}{\partial t}\left(\alpha_{G,i}\rho_G Y_{G,i}^X\right) + \nabla\cdot\left(\alpha_{G,i}\rho_G \mathbf{u}_G Y_{G,i}^X\right) = \nabla\cdot\left(\alpha_{G,i}\rho_G D_G^{eff,X}\nabla Y_{G,i}^X\right) + S_{G,i}^X + \Gamma_{G,i}^X , \tag{7}$$

$$\frac{\partial}{\partial t}\left(\alpha_L\rho_L Y_L^X\right) + \nabla\cdot\left(\alpha_L\rho_L \mathbf{u}_L Y_L^X\right) = \nabla\cdot\left(\alpha_L\rho_L D_L^{eff,X}\nabla Y_L^X\right) + S_L^X + \Gamma_L^X . \tag{8}$$

Here, α denotes the phase fraction and **u** the phasic velocity, both of which are determined by the fluid dynamical part of the model to be discussed shortly. The solvent concentrations are obtained from the constraints $\sum_X Y^X = 1$ for each phase, where a dilute solution is assumed, i.e. the solvent is in large excess. The source terms due to reaction, S^X, and due to transport across the phase interface, Γ^X, as well as the effective diffusion coefficient $D^{eff,X}$ require further modeling as discussed below. For the source terms due to reaction, mass conservation requires that $\sum_X S^X = 0$ for each phase. The mass sources due to transport across the phase interface are related as $\sum_i \Gamma_{G,i}^X = -\Gamma_L^X$ again due to mass conservation. For absorption of species *X*, $\Gamma_L^X > 0$.

For the source terms due to transport across the phase interface we consider the resistance to mass transfer only on the liquid side. Then $\Gamma_{G,i}^X$ is a function of the difference in concentration of the transferred species on the liquid side of the interface and in the bulk liquid. Using Henry's law to relate concentrations on the gas and liquid sides of the interface one gets

$$\Gamma_{G,i}^X = -E_i k_{L,i} a_{I,i} \rho_L \left(He^X Y_{G,i}^X \frac{\rho_G}{\rho_L} - Y_L^X \right). \tag{9}$$

Models for the enhancement factor *E* are described in the next section. The liquid side mass transfer coefficient k_L is modeled in accordance with Darmana et al. (2007) by a correlation due to Brauer (1981) in terms of Reynolds and Schmidt numbers $Re_i = \left|u_L - u_G\right| d_i \rho_L \mu_L^{-1}$ and $Sc = \mu_L\left(\rho_L D_L^X\right)^{-1}$ as

$$k_{L,i} = \frac{D_L^X}{d_i}\left(2 + 0.015\ Re_i^{0.89} Sc^{0.7}\right). \tag{10}$$

The interfacial area concentration a_I can be obtained assuming spherical bubbles as

$$a_{I,i} = \frac{6\alpha_{G,i}}{d_i} . \tag{11}$$

The Henry constant He^X as well as the diffusion coefficient D_L^X are material properties for which correlations are taken from the literature as discussed in appendix A. Liquid density ρ_L and viscosity μ_L are taken as constants for the pure solvent assuming dilute solution. The gas density ρ_G is also taken as a constant corresponding to room conditions since pressure variations are small.

The effective diffusion coefficient for the continuous liquid phase is the sum of a molecular contribution $D_L^{mol,X}$ and a turbulent contribution $D_L^{turb,X}$. The latter is calculated from the turbulent kinematic viscosity by means of a turbulent Schmidt number for which the simple but frequently used assumption is made to take it as unity (e.g. Cockx et al., 2001), i.e.

$$Sc_L^{turb,X} = \frac{\nu_L^{turb}}{D_L^{turb,X}} = 1. \tag{12}$$

The turbulent kinematic viscosity ν_L^{turb} is determined by the fluid dynamical part of the model. The molecular diffusivity $D_L^{mol,X}$ is a material property and correlations for the present material system are given in appendix A. However, in the bulk liquid its contribution is typically negligible compared with the turbulent diffusivity.

For the dispersed gas phase no diffusive transport occurs between bubbles so we set $D_G^{eff,X} = 0$.

Turning now to the fluid dynamical part of the model, an individual continuity equation is solved for each size group *i = 1 ... M*, but a single momentum equation holds for the entire gas phase. For the liquid phase one equation for the conservation of mass and one for the conservation of momentum are required. These equations read

$$\frac{\partial}{\partial t}\left(\alpha_{G,i}\rho_G\right) + \nabla\cdot\left(\alpha_{G,i}\rho_G\mathbf{u}_G\right) = \Omega_{G,i}, \tag{13}$$

$$\frac{\partial}{\partial t}\left(\alpha_G\rho_G\mathbf{u}_G\right) + \nabla\cdot\left(\alpha_G\rho_G\mathbf{u}_G\otimes\mathbf{u}_G\right) = \mathbf{F}_G^{stress} + \mathbf{F}_G^{body} + \mathbf{F}_G^{inter} + \mathbf{F}_G^{masstrans}, \tag{14}$$

$$\frac{\partial}{\partial t}\left(\alpha_L\rho_L\right) + \nabla\cdot\left(\alpha_L\rho_L\mathbf{u}_L\right) = \Omega_L, \tag{15}$$

$$\frac{\partial}{\partial t}\left(\alpha_L\rho_L\mathbf{u}_L\right) + \nabla\cdot\left(\alpha_L\rho_L\mathbf{u}_L\otimes\mathbf{u}_L\right) = \mathbf{F}_L^{stress} + \mathbf{F}_L^{body} + \mathbf{F}_L^{inter} + \mathbf{F}_L^{masstrans}. \tag{16}$$

Here, $\mathbf{F}^{stress}$, $\mathbf{F}^{body}$ and $\mathbf{F}^{inter}$ describe the momentum sources due to internal stress, body forces and interfacial forces. These forces were discussed particularly in the previous validation studies mentioned above, which is why we here concentrate on the extensions related to mass transfer and chemical reaction. In Eqs. (13) - (16) this pertains to the mass sources Ω and the related momentum sources $\mathbf{F}^{masstrans}$. The requirements of overall mass and momentum conservation imply that $\Omega_L = -\sum_i \Omega_{G,i}$ and $\mathbf{F}_L^{masstrans} = -\mathbf{F}_G^{masstrans}$.

According to Rzehak et al. (2016b)[2] the source terms Ω, which appear in the continuity equation (13) of each bubble size group and describe the shrinkage of the bubbles, are given by

[2] On the left hand side of Eq. (2) in Rzehak et al. (2016b) it should read $\alpha_{G,i}$ instead of $\alpha_{G,j}$.

$$\Omega_{G,i} = \frac{m_{B,i}}{m_{B,i} - m_{B,i-1}} \Gamma^X_{G,i} - \frac{m_{B,i}}{m_{B,i+1} - m_{B,i}} \Gamma^X_{G,i+1} \,. \tag{17}$$

There are separate equations for the first and the last bubble size group $i = 1$ and $i = M$, respectively:

$$\Omega_{G,1} = \Gamma^X_{G,1} - \frac{m_{B,1}}{m_{B,2} - m_{B,1}} \Gamma^X_{G,2} \tag{18}$$

and

$$\Omega_{G,M} = \frac{m_{B,M}}{m_{B,M} - m_{B,M-1}} \Gamma^X_{G,M} \,. \tag{19}$$

The transferred mass carries a momentum which is also transferred between the phases. This is given by

$$\mathbf{F}^{masstrans}_G = \mathbf{u}_G \sum_i \Gamma^X_{G,i} \,. \tag{20}$$

Whenever the bubble size is needed in the gas phase momentum equation the mean Sauter diameter over all size groups is used:

$$d_B = \frac{1}{\sum_i \frac{\alpha_{G,i}}{d_i \alpha_G}} \,. \tag{21}$$

3.2 Reactions of CO2 in aqueous NaOH

Further discussion requires specification of the system to be considered, namely the reactive absorption of CO_2 in aqueous NaOH. The reactions of CO_2 in aqueous solution are rather well studied (e.g. Wang et al., 2010; Zeebe and Wolf-Gladrow, 2001; Stumm and Morgan, 1996). A diagram of the reaction network is shown in Figure 2. It can be seen that there are two pathways, where the initial reaction is between the dissolved CO_2 and either hydroxide ions or water, respectively. Both result in a formation of bicarbonate ions which further react to form carbonate ions. It should be noted that the hydration reaction in the second branch can proceed either directly or via the formation of carbonic acid (Eigen et al., 1961). However, because it is neither possible nor necessary to distinguish between these two possibilities, it has been customary to simplify them to a single overall reaction (e.g. Sugai-Guérios et al., 2014; Johnson, 1982; Eigen et al., 1961) as shown on the diagram in Figure 2. Here, the hydroxylation of CO_2 is denoted by a superscript I, the consecutive reaction which results in the formation of carbonate ions by a superscript II, and the hydration of CO_2 by a superscript III. Forward reactions are denoted by a superscript + and backward reactions by a superscript −.

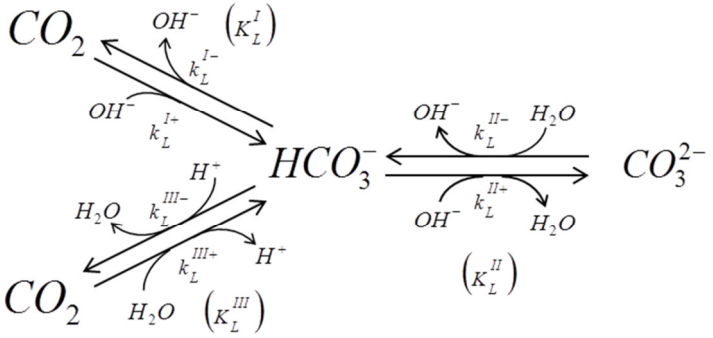

Figure 2: Reaction scheme of CO2 in aqueous solution.

The relative importance of the two pathways, i.e. hydroxylation and hydration, depends on the pH-value. Only the hydroxide path was considered by Darmana et al. (2007), which dominates for pH > 10 (Kern, 1960).
It consists of two steps

$$CO_2 + OH^- \rightleftharpoons HCO_3^- , \tag{22}$$

which can be considered as irreversible, but proceeds at a finite rate, and

$$HCO_3^- + OH^- \rightleftharpoons CO_3^{2-} + H_2O , \tag{23}$$

which takes place instantaneously, but is reversible (Kern, 1960; Pinsent et al., 1956).
If the equilibrium of the second reaction Eq. (23) lies far on the right hand side, which may be expected due to the high pH-values in the initial stage of the chemisorption process, this process may be described by a single irreversible overall reaction

$$CO_2 + 2\,OH^- \rightarrow CO_3^{2-} + H_2O \tag{24}$$

The water path becomes important at pH < 10 and even dominant at pH < 8 (Kern, 1960). It also consists of two steps, the first of which, namely

$$CO_2 + H_2O \rightleftharpoons HCO_3^- + H^+ , \tag{25}$$

is reversible (Knoche, 1980; Kern, 1960)**.** The second step is the same as for the hydroxide path, i.e. Eq. (23).
Both pathways are coupled by the auto-dissociation of water

$$H_2O \rightleftharpoons OH^- + H^+ , \tag{26}$$

which takes place instantaneously (Eigen, 1964).
Using the notation introduced in Figure 2, the reaction rates $R_L^{\Xi\pm}$ may be written as

$$R_L^{I+} = k_L^{I+} C_L^{CO_2} C_L^{OH^-} \tag{27}$$

$$R_L^{I-} = k_L^{I-} C_L^{HCO_3^-} \tag{28}$$

$$R_L^{II+} = k_L^{II+} C_L^{HCO_3^-} C_L^{OH^-} \tag{29}$$

$$R_L^{II-} = k_L^{II-} C_L^{CO_3^{2-}} \tag{30}$$

$$R_L^{III+} = k_L^{III+} C_L^{CO_2} \tag{31}$$

$$R_L^{III-} = k_L^{III-} C_L^{HCO_3^-} C_L^{H^+} = k_L^{III-} C_L^{HCO_3^-} \frac{K_W}{C_L^{OH^-}} . \tag{32}$$

Note that $R_L^{\Xi\pm}$ is always in units of [kmol m^{-3} s^{-1}], but units of the rate constant $k_L^{\Xi\pm}$ depend on the reaction order. In Eqs. (30) and (31) it is assumed that the solvent, H_2O, is present in large excess so that its concentration does not change appreciably during the reaction. Due to the ionization of water with its equilibrium constant K_W the molar concentration of hydrogen ions in Eq. (32) can be replaced by the concentration of hydroxide ions as shown above. A model for the rate and equilibrium constants in this reaction system is detailed in appendix A**.**

The chemical species involved in the process are listed in Table 2. Na^+ does not participate in the reactions, but its presence has to be considered in reaction rates and material properties. The source terms due to reaction, S_L^X in Eq. (8), are given in Table 2 in terms of the reaction rates Eqs. (27) – (32). Since all reactions occur in the liquid, $S_{G,i}^X = 0$ in Eq. (7). The source term due to transport across the phase interface, $\sum_i \Gamma_{G,i}^X = -\Gamma_L^X$ in Eqs. (7) and (8), appears only for the unreacted CO_2. Effects of the chemical reaction on the mass transfer are included in this term by means of an enhancement factor, which may be obtained from either film, penetration, or renewal models as described below. Once the CO_2 is dissolved in the water no further distinction is made between film and bulk liquid such that a seamless treatment of fast and slow reaction is possible.

X	S_L^X	Γ_L^X
CO_2	$M^{CO_2}(-R^{I+}+R^{I-}-R^{III+}+R^{III-})$	$\neq 0$
$(Na^+)OH^-$	$M^{OH^-}(-R^{I+}+R^{I-}-R^{II+}+R^{II-}-R^{III+}+R^{III-})$	0
$(Na^+)HCO_3^-$	$M^{HCO_3^-}(+R^{I+}-R^{I-}-R^{II+}+R^{II-}+R^{III+}-R^{III-})$	0
$(2Na^+)CO_3^{2-}$	$M^{CO_3^{2-}}(+R^{II+}-R^{II-})$	0

Table 2: Summary of species and source terms for the absorption of CO_2 in aqueous NaOH.

3.3 Enhancement factor models

The enhancement factor is defined as the ratio between mass fluxes through the phase interface with and without reaction, based on the same driving force of concentration (e.g. Danckwerts, 1970; Westerterp et al., 1987). It is usually derived based on film-, penetration-, or renewal models of mass transfer. The resulting expressions contain concentrations in the liquid right next to the phase interface, $C_{L,I}^X$, and concentrations representative of the bulk liquid, $C_{L,\infty}^X$, as parameters. For use with the Euler-Euler simulations described above, the latter are identified with the local liquid concentrations C_L^X while the former are calculated from the local gas concentrations C_G^X using Henry's law.

Obviously the enhancement factor depends on the type of reaction that occurs. For the conditions of Darmana et al. (2007), it suffices to consider the overall reaction Eq. (24) which is of the form A + ν^B B $\rightarrow$ P, where A corresponds with CO_2, B with OH^-, and P with CO_3^{2-}.

The stoichiometric factor of OH^- in this reaction is $\nu^B = 2$, but the reaction is still of first order in both reactants. The Hatta number thus is

$$Ha = \frac{\sqrt{k_L^{I+} D_L^A C_L^B}}{k_L}. \tag{33}$$

Because of the irreversibility, the products P do not matter. To keep the notation clear, we here and in the rest of this section suppress the dependence of k_L, Ha, and E on the index of the bubble size group, i.

An expression for the enhancement factor for this case has been derived by DeCoursey (1974) based on the renewal model as

$$E = -\frac{Ha^2}{2(E_a - 1)} + \sqrt{\frac{Ha^4}{4(E_a - 1)^2} + E_a \frac{Ha^2}{(E_a - 1)} + 1}. \tag{34}$$

This expression was used by Darmana et al. (2007) and as shown in Krauß and Rzehak (2016), differences to alternative expressions derived from the film and penetration models are only minor for a large range of Hatta number, Ha, and the asymptotic limiting value for an instantaneous reaction, E_a.

Unless the condition $E_a \geq 1$ is violated, Eq. (34) will always give values for E which are greater or equal to one. Otherwise values are limited by using $\max(E,1)$ (Westerterp et al., 1987).

A solution to the purely diffusional problem of the asymptotic limit of an instantaneous reaction of the above type, which applies to both the penetration and renewal models, has been given by Danckwerts (1970) as

$$\begin{aligned} E_a &= \frac{1}{\operatorname{erf}\left(\beta / \sqrt{D_L^A}\right)} \\ &= \frac{\operatorname{erf}\left(\beta / \sqrt{D_L^B}\right)}{\operatorname{erf}\left(\beta / \sqrt{D_L^A}\right)} + \frac{\exp\left(-\beta^2 / D_L^B\right)}{\exp\left(-\beta^2 / D_L^A\right)} \frac{C_{L,\infty}^B}{\nu^B C_{L,I}^A} \sqrt{\frac{D_L^B}{D_L^A}}. \end{aligned} \tag{35}$$

Here, in general the second equation needs to be solved for β first, before evaluating the first equation for E_a. Results are shown as the solid lines in Figure 3

An analytical solution is possible for $D^A = D^B$, where β drops out in Eq. (35) and E_a becomes

$$E_a = 1 + \frac{C_{L,\infty}^B}{\nu^B C_{L,I}^A}. \tag{36}$$

For the case $\beta \to 0$ corresponding to $E_a \to \infty$, a direct evaluation of Eq. (35) is also possible by calculating the limit of the first term on the right hand side according to de l'Hôpital's rule (e.g. Jeffrey, 2005). This gives an approximate explicit expression valid for $E_a >> 1$ as

$$E_a = \sqrt{\frac{D_L^A}{D_L^B}} + \frac{C_{L,\infty}^B}{\nu^B C_{L,I}^A} \sqrt{\frac{D_L^B}{D_L^A}} = \left(1 + \frac{D_L^B C_{L,\infty}^B}{\nu^B D_L^A C_{L,I}^A}\right) \sqrt{\frac{D_L^A}{D_L^B}}. \tag{37}$$

This expression is shown as the dashed lines in Figure 3a). For $D^A = D^B$ Eq. (37) agrees with the exact result Eq. (36), but otherwise reasonable accuracy requires $E_a \geq 2 \ldots 10$ depending

on the value of D^A / D^B. In general Eq. (37) is not even guaranteed to satisfy the requirement $E_a \geq 1$. Therefore, the first term is sometimes changed to 1, i.e.

$$E_a = 1 + \frac{C^B_{L,\infty}}{\nu^B C^A_{L,I}} \sqrt{\frac{D^B_L}{D^A_L}}, \tag{38}$$

which gives the black solid line in Figure 3 irrespective of the true value of D^A / D^B. Depending on this value the error may still be significant, but at least it remains bounded as E_a approaches 1. The approximations Eqs. (37) and (38) are frequently quoted in reaction engineering textbooks (e.g. Westerterp et al., 1987), but the error should be carefully checked for each application.

An explicit fit-formula that reproduces the numerical solution of the implicit Eq. (35) with engineering accuracy over a large range of parameters is developed in appendix B. A comparison between both is shown as the dashed lines in Figure 3b).

In the work of Darmana et al (2007), Eq. (37) was used for E_a. However, as will be seen (cf Figure 6 c) in section 4.2), the enhancement factor for the pertinent conditions is less than 2 so that this approximation does not apply. In fact it gives values of E_a which are smaller than 1. Therefore, in the present work, the fit-formula from appendix B will be employed.

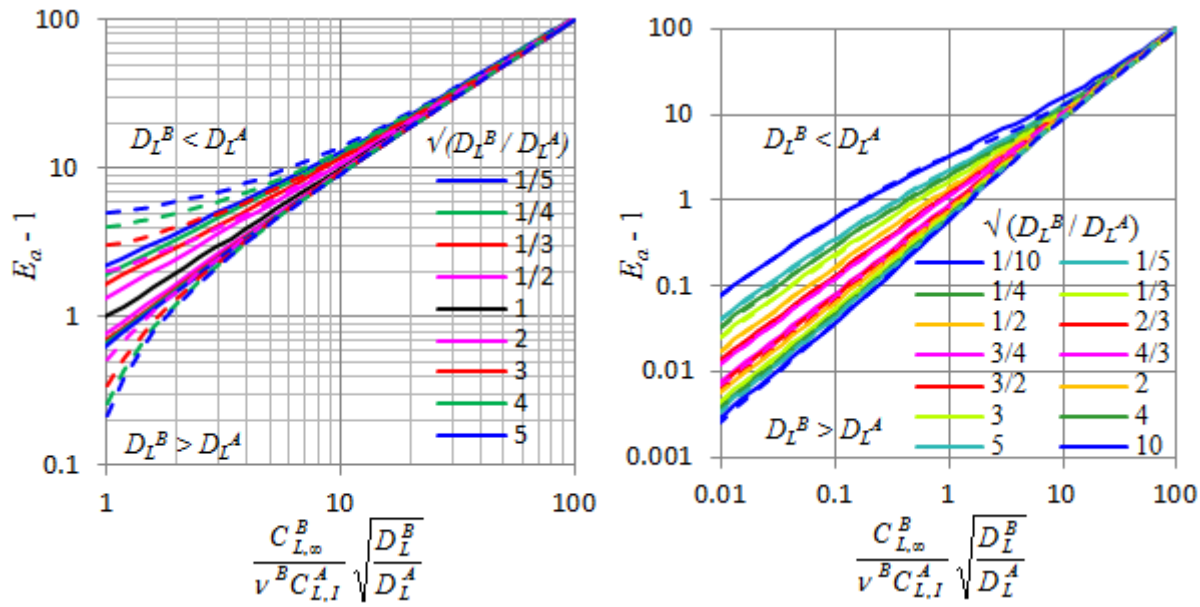

Figure 3: Comparison of expressions for the asymptotic limit of the enhancement factor of an instantaneous second order reaction. a) Solid lines: numerical solution of the implicit equation Eq. (35); dashed lines: explicit approximation Eq. (37). b) Solid lines: numerical solution of the implicit equation Eq. (35); dashed lines: explicit fit formula Eqs. (B.4)-(B.6).

4 SIMULATION RESULTS

Simulations with the Euler-Euler / RANS model of section 3 have been performed for both the non-reactive and the reactive cases using a custom version of ANSYS CFX 14.5. The simulations were run in transient mode on the full 3D domain. The domain was discretized using a uniform rectangular mesh with 29 cells in width, 75 in height and 9 in depth based on a study of the grid-dependence showing that further refinement gives only small changes in the results but enormously increases the computational effort required in particular for the reactive case. For the non-reactive case the time-step was set to $5 \cdot 10^{-3}$ s, which guaranteed that the Courant-Friedrichs-Lewy number was always below 1. For the reactive case smaller time-steps from $2 \cdot 10^{-4}$ s to $1 \cdot 10^{-3}$ s had to be used, depending on the current pH-value. In accordance with Darmana et al. (2007), time-averaged results were calculated during the time intervals $t = 20 - 80$ s and $t = 20 - 95$ s for the non-reactive and the reactive case, respectively.

On the walls a no-slip condition holds for the continuous phase and a free-slip condition for the dispersed phase, assuming that direct contacts between the bubbles and the walls are negligible. To avoid the need to resolve the viscous sublayer, a single phase turbulent wall function assuming a smooth wall was used. For the mass fractions, the normal derivative vanishes on the walls as well as at the outlet at the top of the domain. In addition, a degassing condition was applied there, meaning an outlet condition for the dispersed phase and a free-slip and no-penetration condition for the continuous phase. The inlet, supplying pure nitrogen or carbon dioxide with a bubble diameter of 5.5 mm, was modeled as a rectangular area with a size of close to 30 x 10 mm at the column bottom, where the gas mass flux and the mass fractions are specified.

The continuous phase is considered as a mixture of sodium, hydroxide, bicarbonate and carbonate ions and carbon dioxide dissolved in water. While the initial concentrations of sodium and hydroxide ions were calculated with the initial pH-value of 12.5, all other concentrations were initially set to zero. The gas phase is considered as a mixture of nitrogen and carbon dioxide, to allow the development of the flow using non-reactive nitrogen according to the experiment. The shrinkage of the bubbles due to gas absorption was described by the homogeneous MUSIG model. For this purpose the dispersed phase was divided into 11 size groups with a constant difference in diameter of 0.5 mm.

As already mentioned, in the following the present Euler-Euler / RANS simulations will be compared with both the experiment and Euler-Lagrange / LES simulations of Darmana et al. (2007). In addition for the reactive case a comparison can be made with the simplified model used by Krauß and Rzehak (2016). In this latter approach, all spatial dependences were neglected and only concentrations in the liquid phase were considered. Experimental values were used for the gas fraction, bubble size and relative velocity. In this way, possible errors of the hydrodynamic modeling were excluded so that the description of the chemistry could be assessed in isolation.
For the approach of Krauß and Rzehak (2016), the evolution equations for the species concentrations, Eqs. (7) and (8) of section 3, simplify to

$$\frac{\partial}{\partial t}\left(\alpha_L \rho_L Y_L^X\right) = S_L^X + \Gamma_L^X \,, \tag{39}$$

with all definitions as given previously. It was assumed that the integral gas hold up of 1.2 %, reported by Darmana et al. (2007), represents the gas volume fraction at the measurement point. Moreover, the bubble diameter at this position was estimated as 3.5 mm using the bubble size distribution shown in figure 13 of Darmana et al. (2007). According to the well-

known diagram of Clift et al. (1978), a relative velocity of about 0.23 m/s is expected. Finally, the bubble diameter and gas volume fraction at the measurement point were taken as constant, although both are expected to increase in time, because the absorption process slows down as saturation is approached.
To estimate the error produced by the hydrodynamic modeling, the non-reactive case will be discussed first.

4.1 Non-reactive case: N_2 / aqueous NaOH

In Figure 4 a) lateral profiles of the time-averaged axial component of the gas velocity at y = 750 mm, z = 0 mm are shown. In the experiment and both simulations a clear peak is visible in the center of the column. The present simulation reproduces the peak observed in the experiment very well, but the decrease in velocity towards the walls is somewhat weaker than in the experiment. This leads to a velocity profile that is broader in the present simulation than in the experiment. The decrease predicted by the simulation of Darmana et al. (2007) shows very good agreement with the experimental data, but the maximum in gas velocity is a little bit lower than in the experiment and the present simulation.

A consequence of the on average higher gas velocity for the present simulation is that the mean residence time of the gas bubbles in the column is somewhat too short compared to the experiment. This corresponds with the integral gas holdup of 2.0 % for the present simulation, being somewhat lower than that obtained in the experiment and the simulation of Darmana et al. (2007), namely 2.3 % and 2.2 %.

Comparing in Figure 4 b) the lateral profiles of time-averaged gas fractions at y = 750 mm, z = 0 mm between the present simulation and the simulation of Darmana et al. (2007), considerable differences can be observed. The gas fraction profile for the present simulation is much broader than that for the simulation of Darmana et al. (2007), which is consistent with the broader velocity profile in Figure 4 a). Furthermore, the central value of the gas fraction is higher for the present simulation than for the simulation of Darmana et al. (2007), which explains the slightly higher gas velocity peak for the present simulation.

It may be noted that for the present simulation the values of the gas fraction for most of the profile in Figure 4 b) exceed the integral gas holdup. This must be due to lower gas fractions in other parts of the column. However, due to the lack of experimentally determined local gas fractions, this point cannot be further clarified.

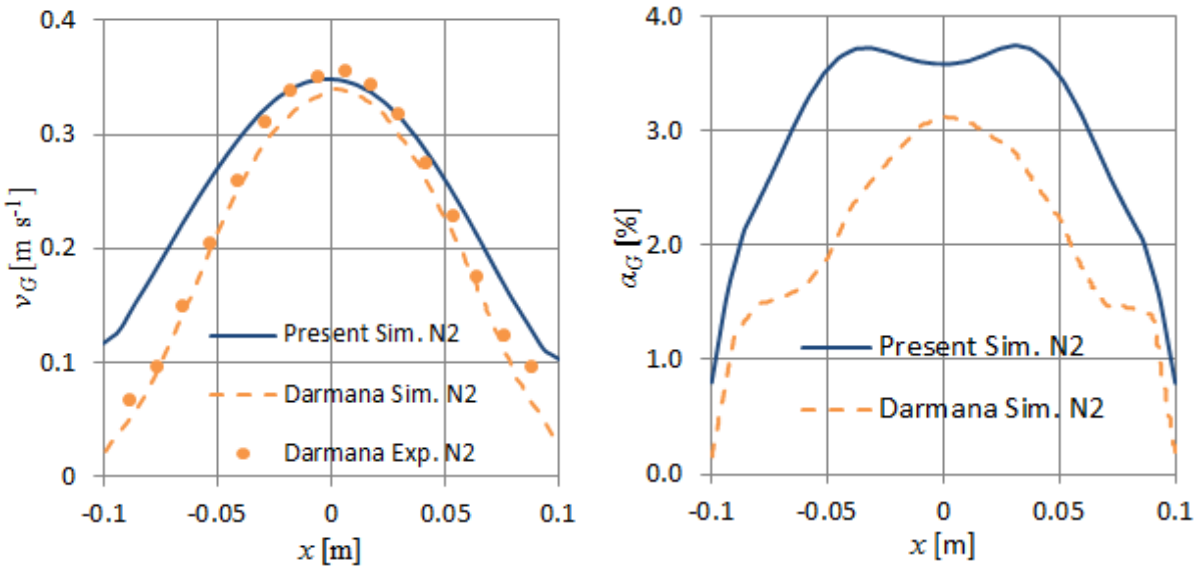

a) b)

Figure 4: Time-averaged lateral profiles for the non-reactive case at y = 750 mm, z = 0 mm. a): axial component of gas velocity; b): gas fraction. Comparison is made as much as possible between the present Euler-Euler / RANS simulation results (solid lines) and the experiment (symbols) and Euler-Lagrange / LES simulation (dashed lines) of Darmana et al. (2007).

Further insight can be gained from the dynamical behavior of the hydrodynamics. In Figure 5 a) the time-dependent axial component of the gas velocity at x = -50 mm, y = 500 mm, z = 0 mm is displayed for the present simulation and the experiment of Darmana et al. (2007). Both curves obviously show periodic oscillations. Such a periodic behavior is characteristic for partially aerated bubble columns and produced by the meandering bubble plume. The oscillation frequency can be determined by applying a discrete Fourier transform, whose results for the present simulation are shown in Figure 5 b). The frequency of the most pronounced oscillation is 0.14 Hz which is somewhat lower than the frequency of 0.17 Hz obtained in the experiment. This experimental value was exactly reproduced by the simulation of Darmana et al. (2007).

As can be seen in Figure 5 a) the simulated minima and maxima are always a bit higher than the experimentally determined ones. This means that in the simulation the gas bubbles are rising faster and are less often and less pronounced carried downwards by the liquid phase. This leads to higher time-averaged gas velocities as shown above and consequently a lower mean residence time and gas holdup.

It is demonstrated that the differences between the experimental data and the present simulation are produced by the not completely exact reproduction of the dynamical flow behavior. Although these differences are not big, the error induced by the pure hydrodynamic modeling should be kept in mind while analyzing the reactive case in the following.

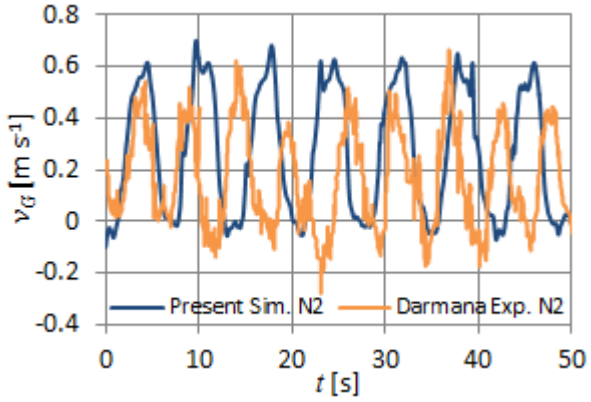

a)

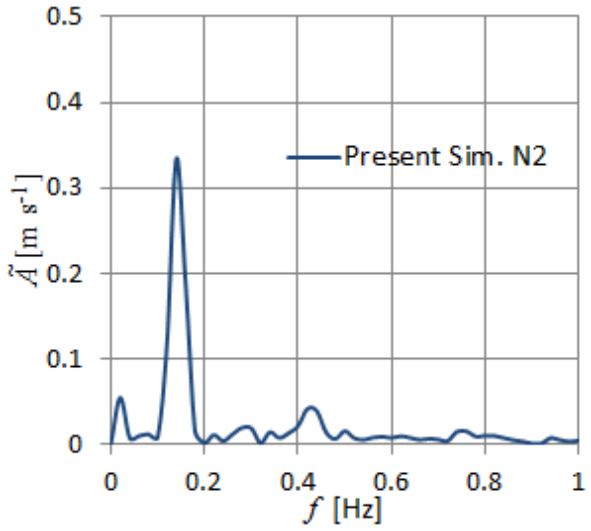

b)

Figure 5: Time-dependent results for the non-reactive case at the point x = -50 mm, y = 500 mm, z = 0 mm. a): Comparison of axial component of gas velocity between the present Euler-Euler / RANS simulation results (dark line) and the experiment (light line) of Darmana et al. (2007). b): Amplitude of Fourier spectrum for the present simulation.

4.2 Reactive case: CO_2 / aqueous NaOH

Quantities which are related to the progress of the chemical reaction are shown in Figure 6, namely the time-dependent pH-values, species concentrations, bubble diameter, and enhancement factor at x = 0 mm, y = 980 mm, z = 0 mm, which is the point of measurement of the pH-value, and the integral gas holdup and gas absorption rate are shown.
A comparison of the time-dependent pH-value obtained from the present Euler-Euler / RANS simulation, the Euler-Lagrange / LES simulation and the experiment of Darmana et al. (2007) and the simplified model of Krauß and Rzehak (2016), mentioned at the beginning of this chapter, is made in Figure 6 a). The high level of agreement between the simplified model and the experimental data could be achieved by using the appropriate enhancement factor model described in section 3.3 and considering both reaction pathways as discussed in section 3.2. Although both improvements to the model used by Darmana et al. (2007) are included in the present simulation, the time-dependent pH-value for the present simulation is quantitatively very similar to that obtained by the simulation of Darmana et al. (2007). However, due to the consideration of the water reaction pathway the curve shape in the later stage of the process matches better with that of the experiment for the present simulation.
As shown in Figure 6 b) the species concentrations of the present simulation and the simulation of Darmana et al. (2007) are completely similar up to a time of ~80 s corresponding to the similarity in pH-values. Subsequently, the process occurs slightly faster in the simulation of Darmana et al. (2007).
From the curve of the time-dependent enhancement factor in Figure 6 c) it can be seen that a chemical enhancement of the mass transfer occurs up to a time of ~80 s. With a maximum value of $E = 1.5$ the enhancement effect is only a moderate one. As long as mass transfer is enhanced by the chemical reactions, the integral gas absorption rate in Figure 6 c) shows its maximum values. When mass transfer enhancement has stopped but still all absorbed gas molecules are consumed by the chemical reactions, a constant concentration gradient between the liquid side phase interface and the bulk liquid and a consequently constant gas absorption rate is reached. After ~180 s the concentration of absorbed CO_2 starts to increase because no reaction partners are available anymore. This results in a decrease in concentration gradient and gas absorption rate.
The more gas is absorbed from the rising bubbles the higher the shrinkage of the bubbles and the higher the decrease in integral gas holdup. Consequently, the curves of the integral gas holdup and the bubble mean Sauter diameter at the measuring point are reciprocal to the gas absorption rate as shown in Figure 6 d).
Overall, the comparison between the simulated and the experimentally determined pH-value reveals a realistic modeling of the chemical reactions but underestimates the mass transfer. Comparing the times at which a neutral pH is reached in simulation and experiment, this underestimation may be roughly estimated as ~20 %. Due to the much better agreement obtained for the simplified model, its cause can be attributed to the hydrodynamics as will be expanded in the following discussion. Agreement between the present simulation and that of Darmana et al. (2007) is viewed as rather accidental with deviations of the latter from the measured data being due to an underestimation of the enhancement effect. This is caused by the use of approximation Eq. (37) for the enhancement factor, which for the diffusivitiy ratio $D^{OH^-} / D^{CO_2} \approx 2.76$ leads to smaller values of E_a than the exact numerical solution of Eq. (35) and the explicit fit formula Eqs. (B.4)-(B.6), as demonstrated in Figure 3.

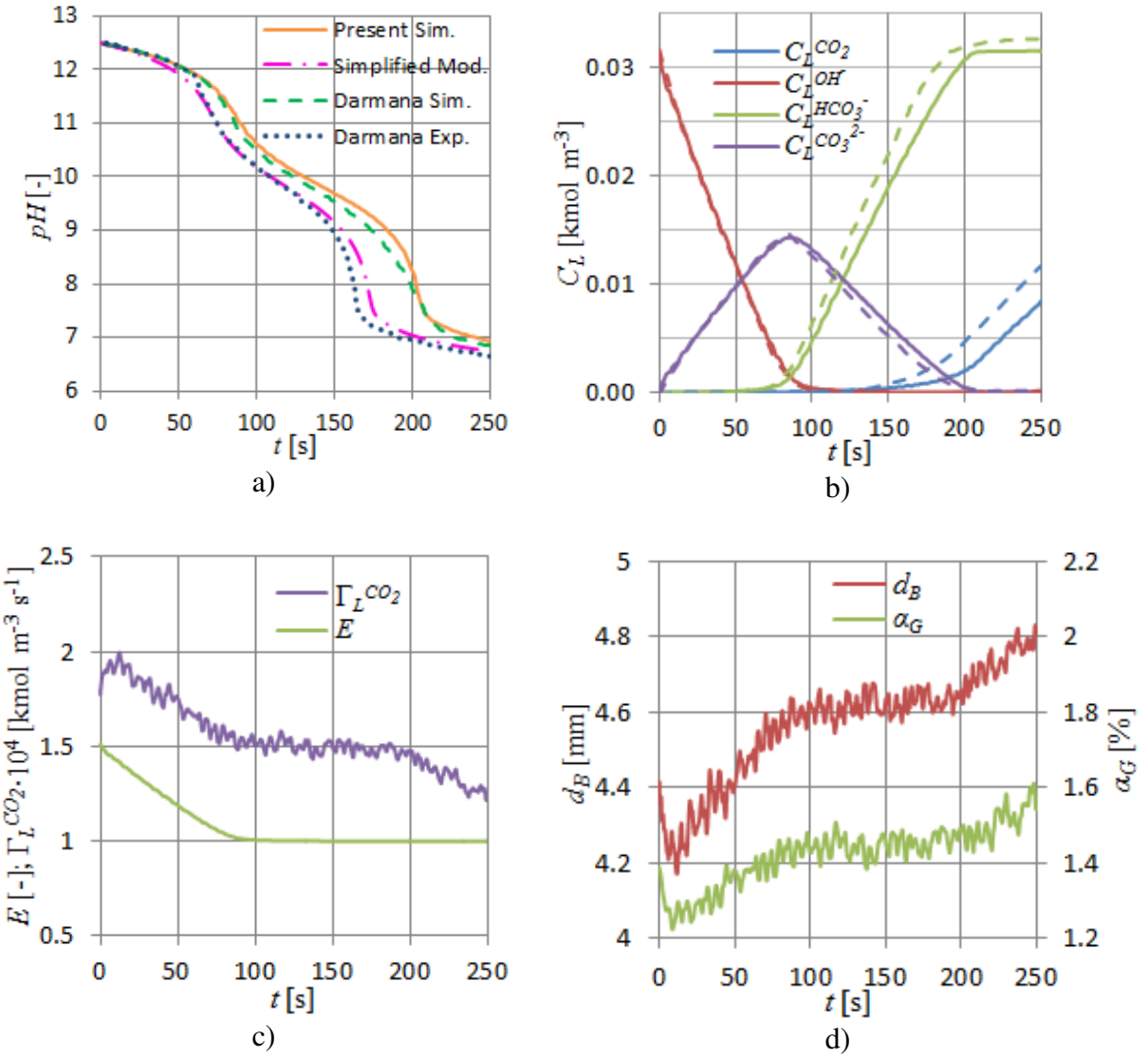

Figure 6: Time-dependent results for the reactive case. a): local pH-value; b): local species concentrations; c): local enhancement factor and integral absorption rate; d): local bubble size and integral gas fraction. Local values are taken at the point x = 0 mm, y = 980 mm, z = 0 mm. Comparison is made as much as possible between the present Euler-Euler / RANS simulation results (solid lines), the results of the simplified model (dash-dotted line) of Krauß and Rzehak (2016) and the experiment (symbols) and Euler-Lagrange / LES simulation (dashed lines) of Darmana et al. (2007).

Figure 7 a) shows a comparison of the time-averaged axial component of the gas velocity at y = 750 mm, z = 0 mm between the present simulation and the simulation and the experiment of Darmana et al. (2007). Additionally, the results of the non-reactive case from section 4.1 are shown for comparison. Again a peak of the gas velocity is obtained in the middle of the column in both simulations and the experiment. Compared to the non-reactive case the height of this peak is clearly reduced due to the shrinking bubbles and consequently lower buoyancy forces. The fact that the peaks in velocity for the simulations are a bit higher than in the experiment indicates that the shrinking of the bubbles is underestimated in both simulations as will be shown shortly.

In accordance with the experiment the decrease in velocity towards the walls becomes flatter for both simulations for the reactive case compared to the non-reactive case. This is because of the bubble shrinkage due to gas absorption and their consequently increased trend to move towards the walls, which is caused by an increased lift force for smaller bubbles. However, the decrease in gas velocity towards the walls in the present simulation is again significantly weaker than in the experiment. Agreement of the simulation of Darmana et al. (2007) with their experiment is similar as for the non-reactive case.

The comparison of the time-averaged gas volume fractions of the present simulation and the simulation of Darmana et al. (2007) in Figure 7 b) shows a higher level of similarity for the reactive case than for the non-reactive case. The gas volume fractions are of the same order now, but the peak in the middle of the column is still more pronounced for the simulation of Darmana et al. (2007), which corresponds with the steeper velocity profile in Figure 7 a). For the present simulation the difference between the gas fractions for the reactive case and the non-reactive case is bigger than for the simulation of Darmana et al. (2007). Since the possibility of a higher mass transfer rate in the present simulation is excluded by the similarity of the curves of the pH-values in Figure 6 a), the differences between both simulations are most likely again related to different gas fractions in not observed parts of the column.

The integral gas holdup of the present simulation of 1.3 % is very close to the experimentally determined one of 1.2 %. In consideration of the discrepancy between the integral gas holdups for the non-reactive case, where the simulated gas fraction is lower than in the experiment, this is likely due to the fact that for the reactive case, the underpredicted residence time of the bubbles in the column is compensated by the ensuing too low mass transfer.

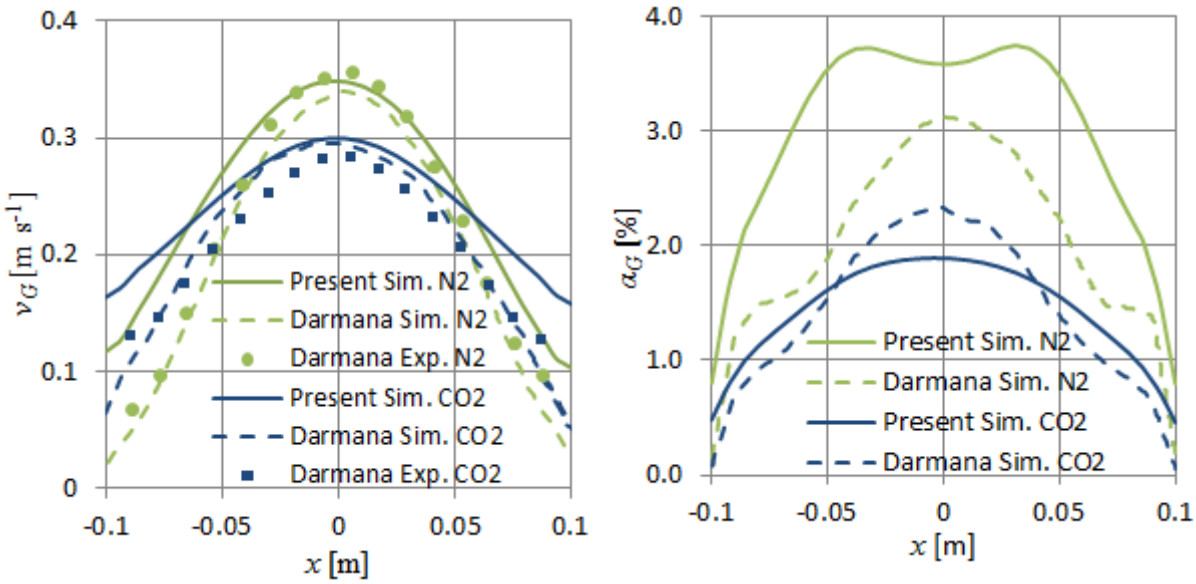

a) b)

Figure 7: Time-averaged lateral profiles for the reactive case at y = 750 mm, z = 0 mm. a): axial component of gas velocity; b): gas volume fraction. Comparison is made as much as possible between the present Euler-Euler / RANS simulation results (solid lines) and the

experiment (symbols) and Euler-Lagrange / LES simulations (dashed lines) of Darmana et al. (2007).

Further comparison is done for the axial development of mean Sauter diameters between the gas inlet and the gas outlet shown in Figure 8. As already mentioned in section 2 the experimental data are judged as unreliable up to a height of ~0.4 m. For both simulations and the experiment a decrease in bubble size with increasing height is observed, which is, of course, due to the gas absorption. In accordance with the underestimation of mass transfer the simulated shrinkage of the bubbles is lower than in the experiment. Nevertheless, the bubble sizes of the present simulation are slightly closer to the experiment than that of the simulation of Darmana et al. (2007).
This demonstrates the general suitability of the application of the MUSIG model in the Euler-Euler two-fluid framework to describe the shrinkage of bubbles due to gas absorption.

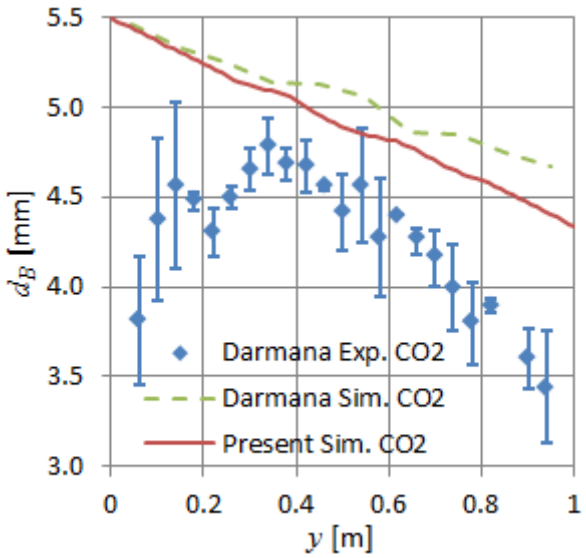

Figure 8: Time-averaged axial profile of bubble mean Sauter diameter for the reactive case at x = 0 mm, z = 0 mm. Comparison is made between the present Euler-Euler / RANS simulation results (solid line) and the experiment (symbols) and Euler-Lagrange / LES simulation (dashed line) of Darmana et al. (2007).

Turning now to dynamical phenomena, Figure 9 a) shows the time-dependent axial component of the gas velocity at x = -50 mm, y = 500 mm, z = 0 mm for the present simulation and the experiment of Darmana et al. (2007). Similar to the non-reactive case a periodically oscillating velocity is observed for both, the simulation and the experiment. While the minima in velocity are almost the same, the simulated maxima and consequently the amplitudes are slightly higher in the simulation than in the experiment. Nonetheless, the differences between the present simulation and the experiment are lower than for the non-reactive case.

The time-dependent velocity is again evaluated by applying a discrete Fourier transform, whose results are shown in Figure 9 b). The frequency of the main oscillation is determined as 0.08 Hz. Similar to the non-reactive case, this frequency is somewhat lower than the frequency of 0.1 Hz observed in the experiment, but closer to it than the frequency of 0.15 Hz in the simulation of Darmana et al. (2007).

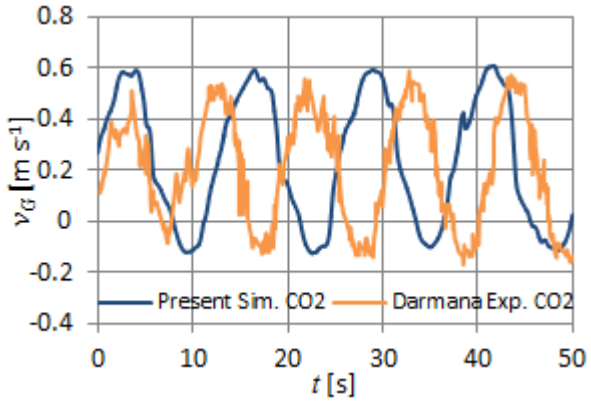

a)

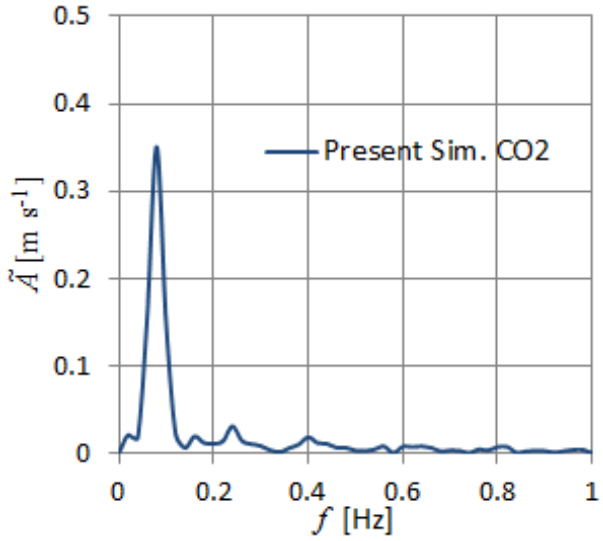

b)

Figure 9: Time-dependent results for the reactive case at the point x = -50 mm, y = 500 mm, z = 0 mm. a): Comparison of axial component of gas velocity between the present Euler-Euler / RANS simulation results (dark line) and the experiment (light line) of Darmana et al. (2007). b): Amplitude of Fourier spectrum for the present Euler-Euler simulation results.

	non-reactive case		reactive case	
	α_G	f_{plume}	α_G	f_{plume}
experiment Darmana	2.3 %	0.17 Hz	1.2 %	0.10 Hz
simulation Darmana	2.2 %	0.17 Hz	1.6 %	0.15 Hz
present simulation	2.0 %	0.14 Hz	1.3 %	0.08 Hz

Table 3: Bubble plume oscillation frequency and integral gas holdup of the present Euler-Euler / RANS simulation, the Euler-Lagrange / LES simulation and the experiment of Darmana et al. (2007) for the reactive and non-reactive cases.

The frequencies of the bubble plume oscillation and the integral gas holdups for both simulations and the experiment of both cases are summarized in
Table **3**. Apart from the decrease in gas holdup, the bubble plume oscillation frequency is reduced when gas is absorbed. This is caused by the reduction of the superficial gas velocity which lowers the bubble plume oscillation frequency (e.g. Buwa and Ranade, 2002). The higher the frequency the higher the number of meanders of the bubble plume in the column and the higher the mean residence time of the gas bubbles. Because the frequency simulated here is a bit too low, bubbles leave the column too fast. Furthermore, a lower frequency of the oscillating bubble plume causes a weaker mixing of the chemical species. Both effects contribute to a slower progress of the mass transfer as observed.

5 DISCUSSION AND CONCLUSIONS

An Euler-Euler / RANS model for the chemisorption of CO_2 in an aqueous solution of NaOH in a bubble column has been investigated in detail. For the fluid dynamics a model validated previously for a range of conditions has been used. A description of mass transfer and chemical reaction was added for the purpose of the present work. Models for the enhancement factor and reaction kinetics were selected based on a previous study using a pointwise calculation that neglects all spatial dependences and makes use of measured values for the bubble size and gas fraction at the measurement point.

Comparison has been made with experimental data and Euler-Lagrange / LES simulations from Darmana et al. (2007) as well as results from the aforementioned pointwise model. A similar degree of agreement with the data was found for the simulations, both of which gave a somewhat too slow decrease of the pH-value. However, the reasons for this deviation are different for both approaches. In the simulations of Darmana et al. (2007), these come from the chemical part of the model, in which an approximate expression for the asymptotic limit of the enhancement factor in case of an instantaneous reaction was used outside its range of validity and the reaction of CO_2 with water was not taken into account. In the present simulations the deviation stems from the fluid dynamical part of the model which gives a too short residence time of the bubbles and, hence, too low mass transfer. This latter conclusion is confirmed by the fact that the pointwise model, for which the chemical part is exactly identical, but bubble size and gas fraction are taken from the experiment, gives a quite good agreement with the pH-measurement.

Since the Euler-Lagrange / LES approach of Darmana et al. (2007) seems to give a better description of the bubble column fluid dynamics, a key to improve the present Euler-Euler / RANS model is likely the turbulence modeling. For partially aerated bubble columns as considered here the shear-induced turbulence typically dominates over the bubble-induced contribution (Ziegenhein et al. 2017). The former is generally captured more accurately by LES than by RANS, while a good description of the latter has been a focus of the present modeling so far (Rzehak and Krepper, 2013b). A comparison of different approaches to turbulence modeling in bubble column flows (Ekambara and Dhotre, 2010) suggests that capturing the anisotropic behaviour of the turbulent fluctuations is most important. Results of that comparison showed that the turbulent kinetic energy was very well described by LES, and a full anisotropic Reynolds-stress model was applicable with a minor loss in accuracy while isotropic two-equation models gave significant errors in that quantity. For a generally applicable model of bubbly flows, the key issue will then be to develop suitable anisotropic source terms for the bubble-induced turbulence (Colombo and Fairweather, 2015).

Other possible causes for the observed deviations are wall effects from the front and back sides, which could be effective due to the thin geometry of the bubble column investigated here. Such effects are not yet included in the present models for the interfacial forces.

A final aspect deserving further attention is the mass transfer coefficient in Eq. (10). The correlation used here is based on investigations of single bubbles and leads to mean values of about $2.5 \cdot 10^{-4}$ m s^{-1} for the present case. Bubble swarm effects, turbulence and other effects, which can significantly influence the mass transfer, are not considered herein so that this value could be somewhat too small. For future numerical investigations of mass transfer other models for the calculation of the mass transfer coefficient should be tested (e.g. Rzehak, 2016), after the dynamical behavior of the fluid-dynamics can be captured with a high accuracy.

6 ACKNOWLEDGEMENT

This work has been carried out in the frame of a research project (GZ: RZ 11/1-1) within the DFG Priority Programme 1740: “Reactive Bubbly Flows” funded by the DFG.

7 APPENDIX A: REACTION AND MATERIAL MODEL

A model for the kinetics of the reaction Eqs. (27) - (32), diffusivity and solubility of the reactants as well as viscosity, density and surface tension of the solvents is presented in the following. It contains the dependence on temperature and ionic effects as much as available from the literature, The development extends the model proposed by Darmana et al. (2007) along the lines of Rzehak and Krepper (2016) and Krauß and Rzehak (2016). Compared with the original references from which the correlations have been taken, some adjustments have been made to obtain consistent units and a sensible number of significant digits in numerical parameter values.

7.1 Viscosity, Density, and Surface Tension

In the dilute limit, the properties of the liquid phase remain those of pure water. The IAPWS (http://www.iapws.org/) provides a highly accurate description thereof which is valid over a very large range of conditions. Numerical values can be obtained from NIST (http://webbook.nist.gov/chemistry/fluid/). However, sometimes it may be useful to have simpler correlations with a smaller range of applicability to work with.

For the viscosity the Vogel-Fulcher-Tammann type formula

$$\mu_L^{H2O} = \exp\left(3.184 + \frac{570.6[\mathrm{K}]}{\mathrm{T} - 140[\mathrm{K}]}\right) \cdot 10^{-6} \cdot [Pa\ s]. \tag{A.1}$$

furnishes such a relation. For the density a quadratic fit can be applied according to

$$\rho^{H2O} = \left(-0.0035 \cdot (\mathrm{T}/[K])^2 + 1.724 \cdot (\mathrm{T}/[K]) + 763.42\right) \cdot [kg\ m^{-3}]. \tag{A.2}$$

According to Rzehak and Krepper (2016) these are valid for temperatures in the range from 5 … 350 °C and pressures up to 10 MPa.

Data on the temperature dependence of surface tension of CO_2 in water can be found in Chun and Wilkinson (1995). Correlations have not been proposed in these works, but as shown by Rzehak and Krepper (2016) a linear fit

$$\sigma^{CO2} = \left(118.31 - 0.158\ T/[K]\right) \cdot 10^{-3} \cdot [N/m]. \tag{A.3}$$

provides a good match to the data in the temperature range from 5 … 350 °C. However, this holds only at atmospheric conditions while at higher pressures a very different behavior is seen (Hebach et al. 2002) which is caused by the increased adsorption of dissolved CO_2 at the interface (Jho et al. 1978).

7.2 Solubility

Under the condition of low solute concentration, the solubility of CO_2 in water is described by a Henry constant *He*. From different definitions in use, the dimensionless ratio of the concentration in the liquid to the concentration in the gas at equilibrium is the most convenient for the present purpose. A correlation for the temperature-dependence in pure water has been given by Versteeg and van Swaaij (1988) based on own measurements as

$$He_W^{CO2} = 3.54 \cdot 10^{-7}\, RT \exp\left(\frac{2044[K]}{T}\right) \cdot [mol\ J^{-1}]. \tag{A.4}$$

A more complex expression has been given in a comprehensive literature review by Crovetto (1991) for which validity up P = 1 MPa has been ascertained. Since deviations between both are restricted to temperatures close to 0°C the simpler expression Eq. (A.4) has been used herein following Rzehak and Krepper (2016).

Due to the salting-out effect in electrolytic solutions, the solubility of most gases is decreasing with increasing salt concentration. Weisenberger and Schumpe (1996) presented a method which is able to predict the solubility of different gases in different salt solutions by extension of a model developed by Schumpe (1993). The resulting expression is

$$He^{CO_2} = He_W^{CO_2} 10\text{^}\left(-\sum\left(h^I + h^A\right) C_L^I\right), \tag{A.5}$$

where $h^A = h_0^A + h_T^A \cdot \left(T - 298.15[K]\right)$. The required constants for the discussed system can be found in
Table A.**1**.

Ion	h^I [m^3 kmol^{-1}]	Gas	h_0^A [m^3 kmol^{-1}]	h_T^A [m^3 kmol^{-1} K^{-1}]
Na^+	0.1143	CO_2	-0.0172	$-0.338 \cdot 10^{-3}$
OH^-	0.0839			
HCO_3^-	0.0967			
CO_3^{2-}	0.1423			

Table A.1: Parameters for Eq. (A.5).

7.3 Diffusivity

The temperature dependence of the molecular diffusivity of CO_2 in water has also been correlated by Versteeg and van Swaaij (1988) based on a review of earlier literature data as

$$D_W^{CO_2} = 2.35 \cdot 10^{-6} \exp\left(\frac{-2119\ [K]}{T}\right) \cdot \left[m^2 s^{-1}\right]. \tag{A.6}$$

More recent data have been provided by Frank et al. (1996) which match Eq. (A.6) as well. All of these data have been taken at atmospheric pressure. Data of Lu et al. (2013) at P = 20 MPa still fall within the scatter of the atmospheric pressure values. Since all data match very well with the correlation Eq. (A.6), this is adopted for the present work again following Rzehak and Krepper (2016).
The molecular diffusivity of CO_2 in electrolytic solutions containing relatively small ions in moderate concentrations can be calculated with a method suggested by Ratcliff and Holdcroft (1963) as

$$D^{CO_2} = D_W^{CO_2}\left(1 + 0.624 \sum b^I C_L^I\right). \tag{A.7}$$

The required constants b^I are shown in
Table A.**2**.

Ion	b^I [m^3 $kmol^{-1}$]
Na^+	-0.0857
OH^-	-0.1088
HCO_3^-	-0.1150
CO_3^{2-}	-0.2450

Table A.2: Parameters for Eq. (A.7).

The temperature dependent molecular diffusion coefficients of the other species in solution are determined by power-law fits of the type

$$D^I = D_0^I \left(\frac{T}{T^I} - 1 \right)^{\gamma^I} , \tag{A.8}$$

as suggested by Zeebe (2011). The constants D_0^I, T^I, and γ^I are given in

Table A.**3**. For bicarbonate and carbonate ions these have been found by Zeebe (2011) from fits to molecular dynamics simulation results. The constants for the sodium ion are obtained by fitting them to the results of a molecular dynamics simulation of Bastug and Kuyucak (2005). The constants for the diffusivity coefficient of hydroxide ions are based on the conductivity measurements of Light et al. (2005). The simulations of Zeebe (2011) and experiments of Light et al. (2005) were performed at infinite dilution. Bastug and Kuyucak (2005) made their simulations for a 0.1 M solution, but give a comparison with experimental data which suggests that the results are also applicable at infinite dilution.

Ion	$D_0^I \cdot 10^9$ [m^2 s^{-1}]	T^I [K]	γ^I [-]
Na^+	5.391	209.7	1.619
OH^-	26.65	216.5	1.658
HCO_3^-	7.016	204.0	2.394
CO_3^{2-}	5.447	210.3	2.193

Table A.3: Parameters for Eq. (A.8).

7.4 Reaction Rate constants

The rate constant of the first forward reaction (Eq. (22)) was investigated by Pohorecki and Moniuk (1988) using a laminar jet technique. They found that it depends on ionic strength and temperature as

$$k_L^{I+} = k_L^{I+,\infty} 10\text{^}\left(0.221 \ \frac{I}{[kmol\ m^{-3}]} - 0.016 \ \frac{I^2}{[kmol^2 m^{-6}]} \right), \tag{A.9}$$

where the temperature dependent rate constant at infinite dilution of ions, $k_L^{I+,\infty}$, is given by

$$k_L^{I+,\infty} = 10\text{^}\left(-\frac{2382\ [K]}{T} + 11.90 \right)\ [\mathrm{m^3\ kmol^{-1}\ s^{-1}}]. \qquad \text{(A.10)}$$

The ionic strength I is defined in terms of the concentration and the valency Z of the dissolved ions

$$I = \frac{1}{2}(C_L^{Na^+} Z_{Na^+}^2 + C_L^{OH^-} Z_{OH^-}^2 + C_L^{HCO_3^-} Z_{HCO_3^-}^2 + C_L^{CO_3^{2-}} Z_{CO_3^{2-}}^2). \qquad \text{(A.11)}$$

Since reaction I plays a role only for pH ≥ 8, at which the concentration of H+ ions is hundered times lower than that of OH- ions, the former have been neglected in this expression.

Pohorecki and Moniuk (1988) also offer a more refined consideration of reaction I in mixed electrolyte systems showing that each ionic species ought to appear with an individual coefficient in the reaction rate, rather than lumped together in terms of the ionic strength. However, the coefficient for one important ion species, namely HCO_3^-, was not determined in their work, so that unfortunately their refined model cannot be used for the present purpose.

The first reaction, Eq. (22), is coupled with the third one, Eq. (25) by the autodissociation of water. Therefore the equilibrium constant K^W of the ionization of water is needed. Tsonopoulos et al. (1976) proposed an equation describing the temperature dependence of K^W as

$$\begin{aligned} K_W &= C_L^{H^+} C_L^{OH^-} \\ &= 10\text{^}\left(-\frac{5840\ [K]}{T} + 55.21 - 22.48\ \lg\left(\frac{T}{[K]}\right)\right) \cdot [kmol^2\ kg^{-2}] \cdot \left(\rho^{H_2O}(T)\right)^2 \cdot \end{aligned} \qquad \text{(A.12)}$$

Considering the equilibrium constant K^{III} of reaction three (Eq. (25)), which is determined from a relation found by Edwards et al. (1978)

$$\begin{aligned} K_L^{III} &= \frac{C_L^{HCO_3^-} C_L^{H^+}}{C_L^{CO_2}} \\ &= \exp\left(\frac{-12090\ [K]}{T} + 235.5 - 36.78\ \ln\left(\frac{T}{[K]}\right)\right) \cdot 10^{-3} \cdot [kmol\ kg^{-1}] \cdot \rho^{H_2O}(T) \end{aligned}, \qquad \text{(A.13)}$$

the backward reaction rate constant of reaction one (Eq. (22)) is obtained as

$$k_L^{I-} = \frac{K^W}{K_L^{III}} k_L^{I+}. \qquad \text{(A.14)}$$

It should be mentioned that for higher concentrations, K^{III} also depends significantly on ionic strength (Millero et al., 2006; Zeebe and Wolf-Gladrow, 2001; Johnson, 1982; Knoche, 1980) which corresponds with the ionic nature of the backward reaction of reaction III (Eq. (25)).

The forward reaction rate constant k_L^{II+} of the second reaction (Eq. (23)) is in the order of $10^{10}\ldots10^{11}$ $\mathrm{m^3\ kmol^{-1}\ s^{-1}}$ as determined by Eigen (1954). This extremely high reaction rate constant is due to the fact that only a proton transfer occurs. As shown by Darmana et al. (2007) a significantly smaller value can be used as long as this reaction remains much

faster than all others, most importantly $k_L^{II+} >> k_L^{I+}$. We have determined that even with $k_L^{II+} = 10^4$ m^3 kmol^{-1} s^{-1} there is negligible influence on the results.
As suggested by Hikita et al. (1976), the equilibrium constant K^{II} of the second reaction considering dependence on the sodium concentration is determined as

$$K_L^{II} = \frac{C_L^{CO_3^{2-}}}{C_L^{OH^-} C_L^{HCO_3^-}} = K_L^{II,\infty} 10\text{^}\left(\frac{1.01 \sqrt{\frac{C_L^{Na^+}}{[kmol\, m^{-3}]}}}{1+1.27 \sqrt{\frac{C_L^{Na^+}}{[kmol\, m^{-3}]}}} + 0.125 \frac{C_L^{Na^+}}{[kmol\, m^{-3}]} \right), \tag{A.15}$$

where

$$K_L^{II,\infty} = 10\text{^}\left(\frac{1567\ [K]}{T} + 0.4134 - 0.006737 \frac{T}{[K]} \right) \left[kmol^{-1} m^3 \right], \tag{A.16}$$

is the temperature dependent rate at infinite dilution of sodium ions.
The backward reaction rate constant k_L^{II-} then is calculated from

$$k_L^{II-} = \frac{k_L^{II+}}{K_L^{II}}. \tag{A.17}$$

Since only uncharged molecules are involved in the third forward reaction (Eq. (25)) the reaction rate constant k_L^{III+} depends on temperature but not ionic strength. According to Johnson (1982) it can be determined as

$$k_L^{III+} = \exp\left(-\frac{6.19 \cdot 10^4 [K]}{T} + 1247 - 183\ \ln\left(\frac{T}{[K]} \right) \right). \tag{A.18}$$

The backward reaction rate constant k_L^{III-} is calculated with the aid of the previously introduced equilibrium constant K^{III} (Eq. (A.13))

$$k_L^{III-} = \frac{k_L^{III+}}{K_L^{III}}. \tag{A.19}$$

8 APPENDIX B: FIT FORMULA FOR THE ENHANCEMENT-FACTOR OF AN INSTANTANEOUS ONE-STEP REACTION OF SECOND-ORDER

As described in section 3.3, the solution of the penetration model for the asymptotic limit of an instantaneous second order reaction results in an implicit expression, Eq. (35), for the enhancement factor E_a. This expression contains two parameters,

$$\chi = \frac{C^B_{L,\infty}}{\nu^B C^A_{L,I}} \sqrt{\frac{D^B_L}{D^A_L}} \tag{B.1}$$

and

$$\delta = \sqrt{\frac{D^B_L}{D^A_L}}\,. \tag{B.2}$$

The numerical evaluation of Eq. (35) shown as the solid lines in Figure 3b) reveals for both small and large values of the parameter χ a linear dependence

$$E_a = 1 + slope\ \chi\,, \tag{B.3}$$

which manifests itself as straight lines with slope one on the log-log plot. Values of the slope determined for small values of the parameter χ are shown in Figure B.1 as a function of $1/\delta$. It may be seen that the slope is close, although not exactly equal, to $1/\delta$.

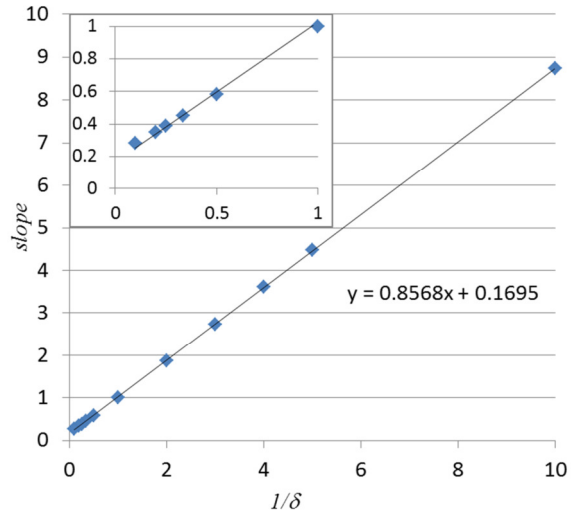

Figure B.1: Slope in Eq. (B.3) determined from the numerical evaluation of Eq. (35) for small values of χ. The inset shows an enlarged view of the region near the origin.

Based on these observations a fit is sought for $(E_a - 1)\ \delta/\chi$. The result for $\delta > 1$ is

$$(E_a - 1)\frac{\delta}{\chi} = 1 + \frac{1}{2}(\delta - 1)\left(\frac{2}{\pi}\arctan\left(0.2\frac{\pi}{2}\ln(\exp(\chi) - 1)\right) + 1\right), \tag{B.4}$$

while for $\delta < 1$

$$(E_a - 1)\frac{\delta}{\chi} = 1 + \frac{1}{2}(\delta - 1)\left(\frac{2}{\pi}\arctan\left(0.2\frac{\pi}{2}\ln\left(\exp\left(\frac{\chi}{\sqrt{\delta}}\right) - 1\right)\right) + 1\right). \qquad \text{(B.5)}$$

Note that for $\delta = 1$ both expressions give the same value

$$(E_a - 1)\frac{\delta}{\chi} = 1, \qquad \text{(B.6)}$$

which coincides with the exact result Eq. (36) for this case.

Here, the function $\ln(\exp(x) - 1)$ maps its arguments, which are always positive, to the entire real line. The function $\frac{2}{\pi}\arctan(\alpha\frac{\pi}{2}x)$ then maps the real line to the finite interval [-1,1], which is finally shifted and scaled to the desired range between 1 for small χ and δ for large χ. The appearance of $\sqrt{\delta}$ in the innermost argument in Eq. (B.5) and the value of $\alpha = 0.2$ were found by trial and error.

The fit formula for $(E_a - 1)\ \delta/\chi$ is compared to results from the numerical evaluation of Eq. (35) in Figure B.2. A comparison for the final results on E_a has been shown in Figure 3. Within a fairly wide range of parameter values, namely

$$0.01 \le \frac{C^B_{L,\infty}}{\nu^B C^A_{L,I}}\sqrt{\frac{D^B_L}{D^A_L}} \le 100 \qquad \textit{and} \qquad 0.01 \le \frac{D^B_L}{D^A_L} \le 100, \qquad \text{(B.7)}$$

the relative deviation between the fit formula and the numerical evaluation of Eq. (35) for E_a is no more than 20%.

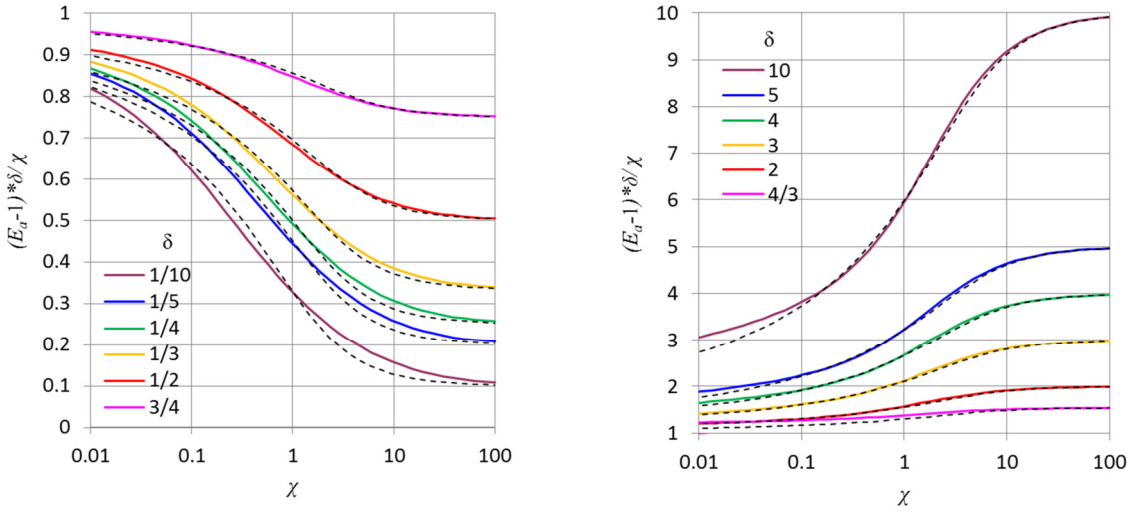

Figure B.2: Comparison of fit formula for $(E_a - 1)\ \delta/\chi$, Eqs. (B.4) – (B.6) (dashed lines) with results from numerical evaluation of Eq. (35) (solid lines).

9 NOMENCLATURE

Notation	Unit	Denomination
a_I	m^{-1}	interfacial area concentration
$\tilde{A}$	$m\ s^{-1}$	amplitude of bubble plume oscillations
C_L^X	$kmol\ m^{-3}$	molar concentration of species X in the bulk liquid
d_B	m	mean Sauter diameter of bubbles
d_i	m	bubble size for *i*-th MUSIG group
D^X	$m^2\ s^{-1}$	diffusion coefficient of species X
E	-	enhancement factor
f	Hz	frequency of bubble plume oscillations
$\mathbf{F}^{body}$	$N\ m^{-3}$	momentum source due to body forces
$\mathbf{F}^{inter}$	$N\ m^{-3}$	momentum source due to interfacial forces
$\mathbf{F}^{masstrans}$	$N\ m^{-3}$	momentum source due to mass transfer
$\mathbf{F}^{stress}$	$N\ m^{-3}$	momentum source due to internal stress
Ha	-	Hatta number
He^X	-	Henry constant for species X
I	$kmol\ m^{-3}$	ionic strength
$k_L{}^{\Xi\pm}$	$(m^3\ kmol^{-1})^{\xi-1}\ s^{-1}$	for- (+) and backward (-) rate constant of reaction Ξ with total reaction order ξ
k_L	$m\ s^{-1}$	mass transfer coefficient
K^{Ξ}	$(m^3\ kmol^{-1})^{\xi^+-\xi^-}$	equilibrium constant of reaction Ξ with total reaction orders $\xi^{\pm}$ for- (+) and backward (-) reaction
K_W	$kmol^2\ m^{-6}$	ionization constant of water
m_i	kg	bubble mass for *i*-th MUSIG group
M	$kg\ kmol^{-1}$	molar mass
R	$J\ K^{-1}\ mol^{-1}$	universal gas constant
$R_L{}^{\Xi\pm}$	$kmol\ m^{-3}\ s^{-1}$	for- (+) and backward (-) rate of reaction Ξ
Re	-	Reynolds number
S^X	$kg\ m^{-3}\ s^{-1}$	mass source of species X due to chemical reactions
Sc	-	Schmidt number
T	K	temperature
$\mathbf{u}$	$m\ s^{-1}$	phase velocity
x	m	coordinate perpendicular to main flow direction
X	-	mole fraction
y	m	coordinate along the main flow direction
Y	-	mass fraction
z	-	coordinate perpendicular to main flow direction
Z^X	-	valency of species X
α	-	phase fraction

Γ^X	kg m^{-3} s^{-1}	mass source of species X due to absorption in equations for species concentration
μ	kg m^{-1} s^{-1}	dynamic viscosity
ν^X	-	stoichiometric factor of species X
ρ^X	kg m^{-3}	mass concentration of species X
$\tilde{\rho}^X$	kg m^{-3}	thermodynamic density of species X
σ	N m^{-1}	surface tension
Ω	kg m^{-3} s^{-1}	mass source due to absorption in fluid dynamic equations

Subscript	**Denomination**
a	asymptotic limit of an instantaneous reaction
B	gas bubble
G	gas phase
i	*i*-th MUSIG group
I	phase interface
L	liquid phase
W	pure water
∞	bulk of a phase

Superscript	**Denomination**
I	first reaction (Eq. (22))
II	second reaction (Eq. (23))
III	third reaction (Eq. (25))
+	forward reaction
-	backward reaction

10 REFERENCES

Bastug, T. and Kuyucak, S., 2005. Temperature dependence of the transport coefficients of ions from molecular dynamics simulations. *Chemical Physics Letters* 408, 84–88.

Bauer, M. and Eigenberger, G., 1999. A concept for multi-scale modeling of bubble columns and loop reactors. *Chemical Engineering Science* 54, 5109–5117.

Bauer, M. and Eigenberger, G., 2000. Multiscale modeling of hydrodynamics, mass transfer and reaction for CO2 chemisorption in bubble column reactors. *16th International Association for Mathematics and Computers in Simulation (IMACS) World Congress*, Lausanne, Swizzerland.

Becker, S., 1996. Experimentelle Untersuchungen von Blasensäulen als Basis für detaillierte Modellrechnungen. *Universität Stuttgart*, Ph. D. thesis (in German).

Brauer, H., 1981. Particle/fluid transport processes. *Progress in Chemical Engineering* 19, 81–111.

Buwa, V. V. and Ranade, V. V., 2002. Dynamics of gas-liquid flow in a rectangular bubble column: experiments and single/multi-group CFD simulations. *Chemical Engineering Science* 57, 4715-4736.

Chun, B.-S. and Wilkinson, G. T., 1995. Interfacial Tension in High-pressure Carbon Dioxide Mixtures. *Industrial and Engineering Chemistry Research* 34, 4371–4377.

Clift, R., Grace, J. R. and Weber, M. E., 1978. Bubbles, drops, and particles. *Academic Press*.

Cockx, A., Do-Quang, Z., Line, A. and Roustan, M., 1999. Use of computation fluid dynamics for simulating hydrodynamics and mass transfer in industrial ozonation towers. *Chemical Engineering Science* 54, 5085–5090.

Cockx, A., Do-Quang, Z., Audic, J., Line, A. and Roustan, M., 2001. Global and local mass transfer coefficients in waste water treatment process by computational fluid dynamics. *Chemical Engineering and Processing: Process Intensification* 40, 187–194.

Colombo, M. and Fairweather, M., 2015. Multiphase turbulence in bubbly flows: RANS simulations. *International Journal of Multiphase Flow* 77, 222 – 243.

Crovetto, R., 1991. Evaluation of Solubility Data of the System CO2–H2O from 273 K to the Critical Point of Water. *Journal of Physical and Chemical Reference Data* 20, 575–589.

Danckwerts, P. V., 1970. Gas-liquid reactions. *McGraw-Hill*.

Darmana, D., Henket, R., Deen, N. and Kuipers, J., 2007. Detailed modelling of hydrodynamics, mass transfer and chemical reactions in a bubble column using a discrete bubble model: Chemisorption of CO2 into NaOH solution, numerical and experimental study. *Chemical Engineering Science* 62, 2556–2575.

DeCoursey, W. J., 1974. Absorption With Chemical Reaction: Development Of A New Relation For The Danckwerts Model. *Chemical Engineering Science* 29, 1867–1872.

Edwards, T. J., Maurer, G., Newman, J. and Prausnitz, J. M., 1978. Vapor-Liquid Equilibria in Multicomponent Aqueous Solutions of Volatile Weak Electrolytes. *AlChE Journal* 24, 966–976.

Eigen, M., 1954. Methods For Investigation Of Ionic Reactions In Aqueous Solutions With Half-times As Short As 10^-9 Sec: Application To Neutralization And Hydrolysis Reactions. *Discussions of the Faraday Society* 17, 194–205.

Eigen, M., Kustin, K. and Maass, G., 1961. Die Geschwindigkeit der Hydratation von SO2 in wäßriger Lösung. *Zeitschrift für Physikalische Chemie* 30, 130–136.

Eigen, M., 1964. Proton Transfer, Acid-Base Catalysis, and Enzymatic Hydrolysis. Part I: Elementary Processes. *Angew. Chem. Int. Ed. Engl.* 3, 1–19.

Ekambara, K. and Dhotre, M., 2010. CFD simulation of bubble column. *Nuclear Engineering and Design* 240, 963-969.

Fleischer, C., Becker, S. and Eigenberger, G., 1996. Detailed Modeling Of The Chemisorption Of CO2 Into NaOH In A Bubble Column. *Chemical Engineering Science* 51, 1715–1724.

Frank, M. J. W., Kuipers, J. A. M., and van Swaaij, W. P. M., 1996. Diffusion Coefficients and Viscosities of CO2+H2O, CO2+CH3OH, NH3+H2O, and NH3+CH3OH Liquid Mixtures. *Journal of Chemical & Engineering Data* 41, 297–302.

Gong, X., Takagi, S., Huang, H. and Matsumoto, Y., 2007. A numerical study of mass transfer of ozone dissolution in bubble plumes with an Euler-Lagrange method. *Chemical Engineering Science* 62, 1081–1093.

Gruber, M. C., Radl, S. and Khinast, J. G., 2015. Rigorous modeling of CO2 absorption and chemisorption: The influence of bubble coalescence and breakage. *Chemical Engineering Science* 137, 188–204.

Hebach, A., Oberhof, A., Dahmen, N., Kogel, A., Ederer, H., and Dinjus, E., 2002. Interfacial Tension at Elevated Pressures - Measurements and Correlations in the Water+Carbon Dioxide System. *Journal of Chemical & Engineering Data* 47, 1540–1546.

Hikita, H., Asai, S. and Takatsuka, T., 1976. Absorption of carbon dioxide into aqueous sodium hydroxide and sodium carbonate-bicarbonate solutions. *The Chemical Engineering Journal* 11, 131–141.

Jain, D., Kuipers, J. A. M., and Deen, N. G., 2015. Numerical modeling of carbon dioxide chemisorption in sodium hydroxide solution in a micro-structured bubble column *Chemical Engineering Science* 137, 685–696.

Jeffrey, A., 2005. Mathematics for engineers and scientists. *Chapman & Hall*, 6th ed.

Jho, C., Nealon, D., Shogbola, S., and Jr., A. K., 1978. Effect of pressure on the surface tension of water: Adsorption of hydrocarbon gases and carbon dioxide on water at temperatures between 0 and 50°C. *Journal of Colloid and Interface Science* 65, 141–154.

Johnson, K. S., 1982. Carbon dioxide hydration and dehydration kinetics in seawater. *Limnology and Oceanography* 27, 849–855.

Kern, D. M., 1960. The hydration of carbon dioxide. *Journal of Chemical Education* 37, 14–23.

Knoche, W., 1980. Chemical Reactions of CO2 in Water. *Biophysics and Physiology of Carbon Dioxide*, *Springer*, 3–11.

Krauß, M. and Rzehak, R., 2016. Reactive absorption of CO2 in NaOH: Detailed study of enhancement-factor models. *Chemical Engineering Science*, submitted.

Liao, J., Ziegenhein, T., and Rzehak, R., 2016. Bubbly flow in an airlift column: a CFD study. *Journal of Chemical Technology & Biotechnology* 91, 2904–2915.

Light, T. S., Licht, S., Bevilacqua, A. C. and Morash, K. R., 2005. The Fundamental Conductivity and Resistivity of Water. *Electrochemical and Solid-State Letters* 8, E16–E19.

Lo, S., 2000. Application of population balance to CFD modelling of gas-liquid reactors. Trends in Numerical and Physical Modelling for Industrial Multiphase Flows, Corse, France.

Lu, W., Guo, H., Chou, I., Burruss, R., and Li, L., 2013. Determination of diffusion coefficients of carbon dioxide in water between 268 and 473 K in a high-pressure capillary optical cell with in situ Raman spectroscopic measurements. *Geochimica et Cosmochimica Acta* 115, 183–204.

Marquez, M. A., Amend, R. J., Carbonell, R. G., Saez, A. E., and Roberts, G. W., 1999. Hydrodynamics of gas-lift reactors with a fast, liquid-phase reaction. *Chemical Engineering Science* 54, 2263–2271.

Millero, F. J., Graham, T. B., Huang, F., Bustos-Serrano, H. and Pierrot, D., 2006. Dissociation constants of carbonic acid in seawater as a function of salinity and temperature. *Marine Chemistry* 100, 80–94.

Pinsent, B. R. W., Pearson, L. and Roughton, F. J. W., 1956. The kinetics of combination of carbon dioxide with hydroxide ions. *Trans. Faraday Soc.* 52, 1512–1520.

Pohorecki, R. and Moniuk, W., 1988. Kinetics of Reaction Between Carbon Dioxide and Hydroxyl Ions in Aqueous Electrolyte Solutions. *Chemical Engineering Science* 43, 1677–1684.

Ramkrishna, D., 2000. Population Balances: Theory and Applications to Particulate Systems in Engineering. *Academic Press*.

Ratcliff, G. A. and Holdcroft, J. G., 1963. Diffusivities of gases in aqueous electrolyte solutions. *Transactions of the Institution of Chemical Engineers* 41, 315–319.

Rzehak, R. and Krepper, E., 2013. Closure models for turbulent bubbly flows: a CFD study. *Nuclear Engineering and Design* 265, 701–711.

Rzehak, R. and Krepper, E., 2013b. CFD modeling of bubble-induced turbulence. *International Journal of Multiphase Flow* 55, 138-155.

Rzehak, R., Krepper, E., Ziegenhein, T. and Lucas, D., 2014. A baseline model for monodisperse bubbly flows. *10th International Conference on CFD in Oil & Gas, Metallurgical and Process Industries* (CFD2014), Trondheim, Norway.

Rzehak, R. and Krepper, E., 2015. Bubbly flows with fixed polydispersity: validation of a baseline closure model. *Nuclear Engineering and Design* 287, 108–118.

Rzehak, R. and Kriebitzsch, S., 2015. Multiphase CFD-simulation of bubbly pipe flow: A code comparison. *International Journal of Multiphase Flow* 68, 135–152.

Rzehak, R., Krepper, E., Liao, Y., Ziegenhein, T., Kriebitzsch, S. and Lucas, D., 2015. Baseline model for the simulation of bubbly flows. *Chemical Engineering and Technology* 38, 1972–1978.

Rzehak, R., Ziegenhein, T., Kriebitzsch, S., Krepper, E., and Lucas, D., 2017. Unified modeling of bubbly flows in pipes, bubble columns, and airlift columns. *Chemical Engineeing Science* 157, 147–158.

Rzehak, R., Kriebitzsch, S. and Krepper, E., 2016b. Euler-Euler Modeling of Hydrodynamics and Mass-Transfer in Bubbly Flows. *Proc. 9th International Conference on Multiphase Flow (ICMF2016)*, Firenze, Italy.

Rzehak, R., Krepper, E., 2016. Euler-Euler Simulation of Mass-transfer in Bubbly Flows. *Chemical Engineering Science* 155, 459-568.

Rzehak, R. 2016. Modeling of Mass-transfer in Bubbly Flows Encompassing Different Mechanisms. *Chemical Engineering Science* 151, 139-143.

Rzehak, R., Krauß, M., Kovats, P., and Zähringer, K., 2017. Fluid Dynamics in a Bubble Column: New Experiments and Simulations. *International Journal of Multiphase Flow* 89, 299–312.

Schumpe, A., 1993. The estimation of gas solubilities in salt solutions. *Chemical Engineering Science* 48, 153–158.

Sugai-Guérios, M. H., Mariano, A. B., Vargas, J. V. C., de Lima Luz, L. F. and Mitchell, D. A., 2014. Mathematical Model Of The CO_2 Solubilisation Reaction Rates Developed For The Study Of Photobioreactors. *Canadian Journal of Chemical Engineering* 92, 787–795.

Stumm, W. and Morgan, J. J., 1996. Aquatic Chemistry: Chemical Equilibria and Rates in Natural Waters. *Wiley*, 3rd ed.

Tsonopoulos, C., Coulson, D. M. and Inman, L. B., 1976. Ionization Constants of Water Pollutants. *Journal of Chemical & Engineering Data* 21, 190–193.

Versteeg, G. F. and van Swaaij, W. P. M. 1988. Solubility and diffusivity of acid gases (CO2 and N2O) in aqueous alkanolamine solutions. *Journal of Chemical & Engineering Data* 33, 29–34.

Wang, X., Conway, W., Burns, R., McCann, N., Maeder, M., 2010. Comprehensive Study of the Hydration and Dehydration Reactions of Carbon Dioxide in Aqueous Solution. *J. Phys. Chem. A* 114, 1734–1740.

Weisenberger, S. and Schumpe, A., 1996. Estimation of Gas Solubilities in Salt Solutions at Temperatures from 273 K to 363 K. *AIChE Journal* 42, 298–300.

Westerterp, K. R., Swaaij, W. P. M. V. and Beenackers, A. A. C. M., 1987. Chemical Reactor Design and Operation. *Wiley*.

Zeebe, R. E. and Wolf-Gladrow, D., 2001. CO_2 in Seawater: Equilibrium, Kinetics, Isotopes. *Elsevier Science*.

Zeebe, R. E., 2011. On the molecular diffusion coefficients of dissolved CO_2, HCO_3^- and CO_3^{2-} and their dependence on isotopic mass. *Geochimica et Cosmochimica Acta* 75, 2483–2498.

Zhang, D.-S., Deen, N. G. and Kuipers, J. A. M., 2009. Euler-Euler Modeling of Flow, Mass Transfer, and Chemical Reaction in a Bubble Column. *Industrial & Engineering Chemistry Research* 48, 47–57.

Ziegenhein, T., Rzehak, R., and Lucas, D., 2015. Transient simulation for large scale flow in bubble columns. *Chemical Engineering Science* 122, 1–13.

Ziegenhein, T., Rzehak, R., Ma, T., and Lucas, D., 2017. Towards a unified approach for modeling uniform and non-uniform bubbly flows. *Canadian Journal of Chemical Engineering* 95, 170–179.